OUKA
Osaka University Knowledge Archive

Title	Computational Study of Forces, Ship Motions and Flow Field for KRISO Container Ship Model in Calm Water and in Regular Head Waves
Author(s)	Hossain, Md. Alfaz
Citation	大阪大学, 2020, 博士論文
Version Type	VoR
URL	https://doi.org/10.18910/77507
rights	
Note	

Osaka University Knowledge Archive : OUKA

https://ir.library.osaka-u.ac.jp/

Osaka University

Doctoral Dissertation

Computational Study of Forces, Ship Motions and Flow Field for KRISO Container Ship Model in Calm Water and in Regular Head Waves

MD. ALFAZ HOSSAIN

June 2020

Department of Naval Architecture and Ocean Engineering
Division of Global architecture
Graduate School of Engineering
Osaka University

Acknowledgements

First and foremost, I would like to express my sincere gratitude to my supervisor, Professor Yasuyuki Toda for providing me the opportunity to become one of his students at Osaka University. It is a privilege to be able to conduct research under his sincere and wise supervision. I am deeply grateful to him for his kind support.

I would like to express my heartiest gratitude to former Assistant Professor Ping-Chen Wu for his continuous support throughout my study, teaching me about this research from the scratch and sharing his scholarly knowledge. Without his friendly and kind assistance and guidance, this study would not be possible.

I would like to thank Dr. Emel Tokgoz, who helped me a lot in my study by providing many necessary resources while I just started this research.

I am wholeheartedly thankful to the Ministry of Education, Culture, Sports, Science and Technology, Japan (MEXT) for supporting me financially.

Furthermore, it is a grace for me to have a wonderful laboratory blessed with fun and supporting members. More especially for those I owe my understanding to: Mr. Kataoka (graduated senior) who was my first Japanese friend and a wonderful tutor, Mr. Truong Quang Tho (graduated senior), Mr. Htike Aung Kyaw (friend, graduated batch mate, study mate), Mr. Kawakami (graduated research mate) and Ms. Seemontini (lab mate).

I would like to thank every single individual who supported me throughout this study.

Finally, yet importantly, I would like to thank my family for of the continuous mental support during my research. I am very grateful to my parents who gave me proper education with all possible facilities throughout my life. I am deeply thankful to my wife who was always there for me with all the mental support during my study and research in Osaka University.

Abstract

Ship motion responses, added resistance and added powering in waves have been predicted by a wide variety of computational tools. However, the validation of the computational flow field is still challenging. This research is a CFD study of the seakeeping and propulsion performance of the KRISO container ship (KCS) model, which is a high Froude number (F_n) ship with low block coefficient C_B, appended with a rudder, with and without propeller condition, in calm water and in regular head waves. The viscous flow simulation was performed by using CFDSHIP-IOWA. The wave conditions proposed in CFD Workshop 2015 were considered, i.e. the wave ship length ratio λ/L =0.65, 0.85, 1.15, 1.37, 1.95 and calm water. The objective is to validate CFD results by EFD data (from the experiment conducted in Osaka University towing tank) for ship vertical motions, added resistance and wake flow field. The detailed flow field for nominal wake and self-propulsion condition have been analyzed for λ/L =0.65, 1.15, 1.37 and calm water. Furthermore, bilge vortex movement and boundary layer development on the propeller plane was compared with the previous research done in our lab for KVLCC2 tanker model. The propeller thrust and wake factor oscillation in waves have been studied as well. The seakeeping and propulsion performance have been compared with the similar CFD work done by FORCE and University of Iowa.

Table of Contents

Nomenclature

A	Amplitude of Incident Waves
AP	Aft Perpendicular of Ship
B	Beam/ Breadth over Waterline
C_B	Block Coefficient
CFD	Computational Fluid Dynamics
D	Depth of Ship
DOF	Degree of Freedom
EFD	Experimental Fluid Dynamics
F_n	Froude Number
FP	Forward Perpendicular of Ship
IIHR	Iowa Institute of Hydraulic Research
I_{yy}	Moment of Inertia in Y-Direction
k	Wave Number
KCS	KRISO Container Ship
KG	Vertical Center of Gravity from ship keel
K_T	Thrust coefficient
K_Q	Torque coefficient
K_{yy}	Radius of Gyration around Y-Axis
L_{PP}	Length between Perpendiculars
LCB	Longitudinal Center of Buoyancy
L_{WL}	Length over Waterline
PF	Potential Flow
PIV	Particle Image Velocimetry
R_e	Reynolds number
T_D	Draft of Ship
T_e	Encounter period
t	Time
U, V, W	Reynolds-averaged velocity components
U_0	Ship Speed

x,y,z	Independent coordinate directions
z	Heave
ζ	Free surface elevation
λ	Wave Length
∇	Displaced Volume of Ship
θ	Pitch
1-w	Effective wake factor
3D	Three Dimensional

List of Tables

List of Figures

Chapter 1: Introduction

1.1 Background

The prediction of ship motion and added resistance is very important as these are directly related to the safe and economic operation of the ship. Ship motion and added resistance of ship are needed to be predicted accurately to assess the seakeeping performances properly. In addition, the fuel consumption of a ship is related to the ship motion and added resistance of the ship. The wake profile and the vortex behavior at the propeller plane have definite influence on the propeller performance and hence on the fuel consumption as well. The Marine Environment Protection Committee (MEPC) of International Maritime Organization's (IMO) has made the regulation for minimum energy efficiency level to be maintained by the seagoing ships. This minimum energy efficiency level is determined by Energy Efficiency Design Index (EEDI) and Energy Efficiency Operational Indicator (EEOI). It is of vital importance to make a reliable prediction of ship motion and added resistance to meet criteria of EEDI and EEOI.

An accurate assessment of ship motion and added resistance is of crucial importance in the process of initial design stage. In the design stage of ship design, engineers must consider ship motion and added resistance. Design engineers can save time and resources by being able to anticipate the ship's performance in early stages. The term "Added Resistance" is used to describe the phenomenon of energy loss because of generation of waves as a consequence of ship motions due to sea waves and the diffraction of waves. The ship speed required power to propeller characteristics are usually estimated for still water conditions. However, during its exploitation, the ship encounters different sea conditions and, in many occasions, the seaway influences the resistance and propulsion features. Modern ships are operated by propeller in stern. The wake profile at the different plane needs to be studied properly to predict the propeller performance, which is related to the fuel consumption of the ship. Ship motion responses, added resistance and added powering in waves have been predicted by a wide variety of computational tools. However, the validation of the computational flow field is still challenging.

1.2 Literature Review

One of the first attempts to obtain the added resistance of a ship was carried out by [Havelock, 1942]. He determined the mean value of the longitudinal component of pressure forces integrated over the wetted part of oscillating ship hull i.e. the increment in resistance in regular waves.

Another relevant contribution to the analytical calculation of added resistance was developed by [Maruo, 1957] [Maruo , 1963]with a potential flow solution. His method is known as drift force method. He considered a control volume around ship hull and then energy and momentum balances were derived. He divided the velocity potential into incident waves, diffracted waves and radiated waves. He obtained the value of diffraction and radiated potentials and the forces on the ship were calculated from the linear momentum flow through a control volume around ship hull. He showed that heave and pitch dominate the effects of surge and therefore he justified neglecting the effect of surge in added resistance.

Radiated energy method was applied by [Gerritsma & Beukelman, 1972]. The method equates the work of added resistance to the energy contained on the damping waves radiated away of the ship.

These are some of the remarkable attempts taken by the researchers to predict the added resistance in early stage. Development of the ship motions and added resistance predictions is a long history and is briefly summarized in [Wu P. C., 2013].

With the rapid advancement of computer technology, CFD has recently become more popular tool to analyze seakeeping performances in viscous flow. By solving Reynolds average Navier-Stokes (RANS) equations, CFD has the advantage of predicting added resistance and ship motions by executing nonlinear computation; no analytical formula for added resistance or empirical values for viscous effect are needed anymore, see [Wu P. C., 2013]. (Carrica, Fu, & and Stern, 2011) used CFDSHIP-IOWA V4.5 for full scale KCS (KRISO container ship) with rudder and rotating discretized propeller in calm water using overset grid. Mean value of motions and force showed good agreement with EFD, but deviated results were observed in their amplitudes and phases. Also, (Castro, Carrica, & and Stern, 2011) used overset grid in CFDSHIP-IOWA V4.5 for full scale KCS with rotating discretized propeller to predict self-propulsion in calm water. Many other

attempts were taken to predict the ship motions and added resistance, using CFD. Remarkable works done by CFD were outlined in [Wu P. C., 2013].

CFDShip-IOWA V4.5 was employed by [Sadat-Hosseini, Wu, Carrica, Kim, Toda, 2013] for the prediction of the motions and added resistance of KVLCC2 at F_n=0.142 and F_n=0.25 with free and fixed surge in short and long head waves using URANS. CFD results were validated against the EFD data for F_n=0.142, provided by Osaka University (free surge condition) and INSEAN (fixed surge condition) for long waves and NTNU for short waves (fixed surge condition). Promising agreement between CFD and EFD was observed in this validation study. It was found that strong correlation exists between the added resistance and the relative bow motion. The study recommended for the bow shape optimization for the possible reduction in added resistance.

Validation study for the prediction of motions and added resistance was carried out by [Simonsen, Otzen, Joncquez, Stern, 2013] for KCS (L=4.367) at F_n=0.26, 0.33 and 0.40 in regular head waves with heave, pitch and roll free conditions. CFD simulations were conducted by RANS solver CFDShip-Iowa. Additional computations were done with the RANS code Star-CCM+ (for λ/L = 1.15 at F_n=0.26 only) and the potential flow code AEGIR (3D B-spline based boundary element code) for comparison. Experiment was conducted in the towing tank at FORCE Technology. Better prediction was made by CFDShip-IOWA than by AEGIR for heave and pitch motion responses. CFDShip-IOWA showed better agreement with EFD data compared to AEGIR for mean added reistance at F_n=0.26, 0.33; whereas underpredictions were observed by both CFDShip-IOWA and AEGIR F_n= 0.40. Star-CCM+ underpredicted the added reistance. It was found that both CFD codes made fair prediction of the 0^{th} harmonic resistance, but underpredicted the 1^{st} harmonic of the resistance.

(Tezdogan, et al., 2015) utilized overset grid in Star-CCM+ to perform a fully nonlinear unsteady RANS simulation to predict the ship motions and added resistance of a full scale KCS. (Filip, Xu, & and Maki, 2017) used Open FOAM for KCS model to predict the ship motions and added resistance in regular and irregular waves.

Towing tank experiment was conducted in FORCE technology [https://forcetechnology.com/en]. Both CFD codes predicted mean resistance fairly, but under predicted the 1st harmonic of the

resistance. Self-propulsion in calm water was predicted using moving mesh in Open FOAM for KCS model by (Gaggero, Villa, & and Viviani, 2015).

Prediction of ship motions and added resistance were done by [Sadat-Hosseini et al., 2015] for KCS at F_n=0.26 in calm water and regular waves for variable wavelength and wave headings. CFDShip-IOWA V4.5 was used for simulation in calm water and head waves [KCS (Case_2.10) , 2015] with heave-pitch free conditions, and in waves with variable headings [KCS (Case_2.11) , 2015] with heave, pitch and roll free conditions. FORCE model (L=6.1 m) was used for the simulations in head waves. For variable wave headings, simulation was carried out for IIHR model (L=2.7 m). To calculate the added resistance, simulations were conducted for both models. Another CFD solver STAR-CCM+ was also used for the simulation in calm water, head waves [KCS (Case_2.10) , 2015] with heave-pitch free conditions using the FORCE model (L=6.1 m). This validation study also involved a Potential Flow (PF) solver, FATIMA. PF computation was done by MARIN and study was carried out without the rudder. PF computations were done in head and variable heading waves, with all 6 DOFs, in general. Experiment was carried out by FORCE (L=6.1 m model) in head waves of variable wavelength with heave-pitch free conditions. IIHR (L=2.7 m model) conducted the experiment in variable headings with heave, pitch, roll and surge free conditions. Large error was observed for CFDShip-IOWA and PF at the peak (λ/L =1.15) for added resistance. The average errors for first harmonic amplitudes and phases were small for both CFD and PF computations, but the errors for the zeroth harmonic of motions were found to be large. The oscillation of nominal wake fraction (w_N) predicted by STAR-CCM+ for λ/L =1.37 was almost sinusoidal with lower mean value than calm water one.

Literature shows that the studies of ship motion responses and added resistance in waves have been carried out by many researchers by a wide variety of methods, but very few studies reflected on the viscous ship wake. It is very important to understand the profile and behavior of viscous ship wake in waves to determine the influence of viscous wake on the propulsion performance of the ship. Hence, the importance to understand the viscous ship wake in waves have been stressed recently by many researchers. Nevertheless, detail research of the wake field inside the propeller plane in waves are done by very few researchers, although the number is increased in recent years; see [Wu P. C., 2013].

Resistance and self-propulsion experiment were conducted by (Nakamura & Naito, 1975) for a single screw high speed container in regular and irregular head waves. A ring type wake meter was used to measure the inflow velocity at the propeller plane. In addition, using this measured inflow velocity, the propeller performance also was calculated by the blade element theory. This study showed that the self-propulsion factors in regular head waves vary considerably with wave length, especially in the range of λ/L = 1.0 ~ 1.5 where ship motions are severe.

Recently, computational study of propeller performance and flow field analysis have been carried out and compared with the EFD results by [Wu, Tokgoz, Okawa, Tamaki, and Toda, 2016] for KVLCC2 tanker in regular head waves at F_n=0.142 for λ/L = 0.6, 1.1 and 1.6. Experiment was carried out at Osaka University Towing tank with free surge, heave and pitch conditions. A new body-force propeller model [Tokgoz, Win, Kuroda, Toda, 2014] was coupled with RANS code CFDShip-IOWA V4.5 for the simulation to analyze propeller performance with fixed surge (free to heave and pitch) condition for diffraction computations. For radiation problem, the simulation was done with 2DOF (forced to heave and pitch) and 1DOF (forced to heave or forced to pitch) conditions. Good prediction compared to the EFD data was observed for thrust time histories, motion responses and the wake field phenomena. The thrust fluctuation shape and mean values of the thrust could be predicted very well by CFD. It was found from the radiation problem results that the ship vertical motions (especially pitch motions) are the major effects for the 2nd harmonic components of the thrust fluctuations. It was concluded that the periodic change of bilge vortex and low speed area below or around the shaft, relative to the ship motions in waves, affected the propeller performance.

(Ozdemir, Cosgun, Dogrul, & and Barlas, 2016) used Star CCM+ 6.06 to predict the nominal wake at the propeller plane of KCS model in calm water. CFDSHIP-IOWA V4.5 has been used by Wu, Hosseini, Stern, and Toda (2017) for the KVLCC2 without propeller (with dummy boss) in fully loaded condition, free to heave and pitch at Fn=0.142. The detailed phenomena of nominal wake behaving in waves were analyzed by studying the velocity distribution and vortex behavior on the propeller plane.

CFDShip-IOWA V4.5 has been used by [Wu, Sadat-Hosseini, Stern, and Toda, 2017] for the KVLCC2 tanker (L= 3.2 m) without propeller (with dummy boss) in fully loaded condition, free

to heave and pitch at F_n=0.142 for λ/L = 0.6, 1.1 and 1.6. The detailed phenomena of nominal wake behaving in waves were analyzed by studying the velocity distribution and vortex behavior on the propeller plane (x/L =0.98). Orbital velocity and the volume average nominal wake velocity were also studied. However, main concentration in this study was to understand the vortex behavior of the nominal wake on the propeller plane. The bilge vortex and the secondary vortex could be observed clearly. It was observed that the bilge vortex moved up and down relative to ship stern movement, even moved out of the propeller radius.

Following the above-reviewed studies, viscous ship wake and thrust oscillation in waves is of great concern to resistance and propulsion. Especially, to validate the computational flow field in waves is still challenging. Compared to our previous studies for KVLCC2 tanker (Sadat-Hosseini, et al., 2013; Wu, et al., 2016; Wu, et al., 2017), in the present work the KCS ship was appended with a rudder in higher Froude number 0.26 and with smaller block coefficient 0.65. The objective is to validate CFD results by EFD data for ship vertical motions, added resistance, thrust, torque, added powering variables and wake flow field. Furthermore, bilge vortex movement and boundary layer development on propeller plane, thrust and wake factor oscillation in waves have be studied. Our results (without propeller case) have been published in (Hossain, Wu, Shibano, & Toda, 2018), along with some preliminary results of self-propulsion computation. Later, all the results, except the added powering, have been published in our recent paper (P.-C., et al., 2020).

Chapter 2: Objective and Conditions

The main objective of this research is to study the propulsion performance of a vessel with high Froude number (F_n) and low block coefficient (C_B) in calm water and in head waves using CFD. As it is stated in the first chapter, in addition of predicting the ship motions and added resistance, reliable predictions of the wake profile and the vortex behavior at various plane are very important to meet the criteria of EEDI and EEOI.

The research content can be divided in two major parts which will help to efficiently describe the objective of the study. At first, the objective is to predict the ship motions and added resistance in calm water and in head waves without propeller condition. In addition, the bilge vortex movement and the boundary layer development at the propeller plane will be studied. All these computational results will be compared with our EFD results for same condition (without propeller) and also with other similar computational results.

In the second part of the study, Osaka University Body Force Propeller Model will be included to consider the propeller effect in the self-propulsion condition. The objective is to analyze the vortex behavior and the velocity field before & after the propeller plane and after the rudder for the self-propulsion condition and compare with the EFD results. The effective wake factor for different wavelength will be studied as well. Moreover, prediction of the thrust and torque value, along with their time history, and comparing these computational results with the EFD values are contained in the research objective. In addition, it was intended to predict the added powering variables and make a comparison with our EFD results as well as the results of other institutions.

The objective ship in this study is the KCS (KRISO Container Ship) which has been conceived to provide data for both explication of flow physics and CFD validation for a modern container ship with bulbous bow as well as recommended in [Tokyo Workshop on CFD in Ship Hydrodynamics, 2015] for CFD validation study.

The main particulars of full scale KCS are shown in Table 1. Service speed for the full scale KCS is 24 knots, corresponding to the F_n= 0.26. Reynolds number (R_e) for the full-scale ship is 2.49×10^9. However, model scale has been used for the simulation and the experiment. The 3.2m KCS model

has been used in Osaka University for the EFD and the same model has been chosen for the CFD validation study. The KCS model is shown in Figure 1. The main particulars of the KCS model are shown in Table 2. The vertical center of Gravity (KG) has been adjusted to 0.199 m for the required K_{yy} with a swinging equipment. Reynolds number (R_e) for the KCS model is 4.1×10^6.

The computational study has been done for the fully loaded condition of the KCS ship with Heave-pitch-free (2DOF) ship motions in calm water and regular waves for the prescribed λ/L ratios in [KCS (Case_2.10) , 2015]. Prescribed λ/L ratios are 0.65, 0.85, 1.15, 1.37 and 1.95. At first, the research has been done without the propeller, but a dummy propeller boss has been included.

Table 1: Main particulars of KCS (full-scale)

Length between perpendiculars: L_{PP} (m)	230.00
Length of waterline: L_{WL} (m)	232.50
Maximum beam of waterline: B (m)	32.20
Depth: D (m)	19.00
Draft: T (m); fully loaded condition	10.80
Displacement volume: ∇ (m^3)	52030.00
Wetted surface area without rudder: S_W (m^2)	9424.00
Wetted surface area of rudder: S_R (m^2)	115.00
Block coefficient (C_B)	0.65
LCB (%L_{PP}), fwd+	-1.48
Radius of gyration (around x axis): K_{XX}	0.4B
Radius of gyration (around y axis): K_{YY}	0.25L_{PP}
Radius of gyration (around z axis): K_{ZZ}	0.25L_{PP}

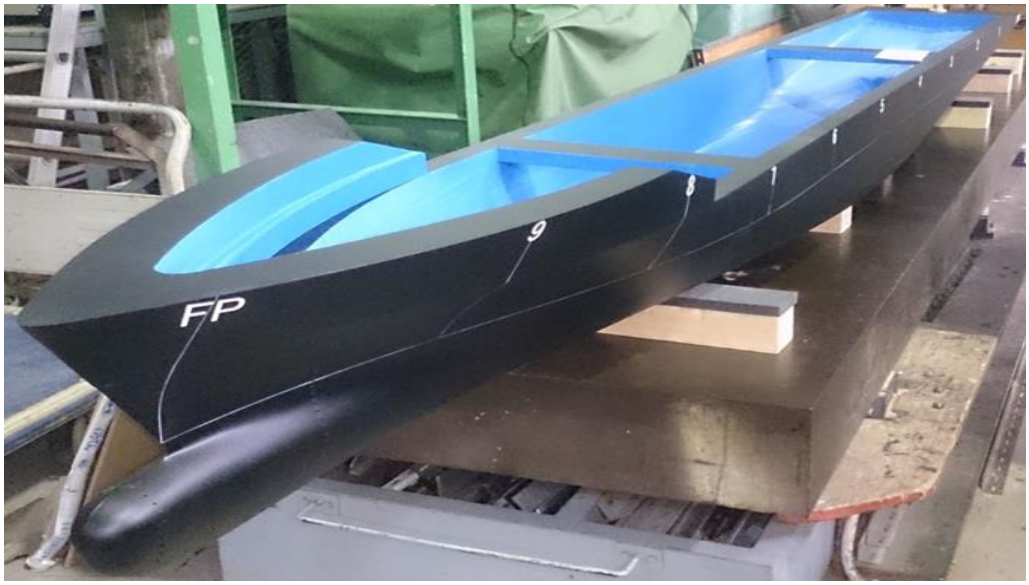

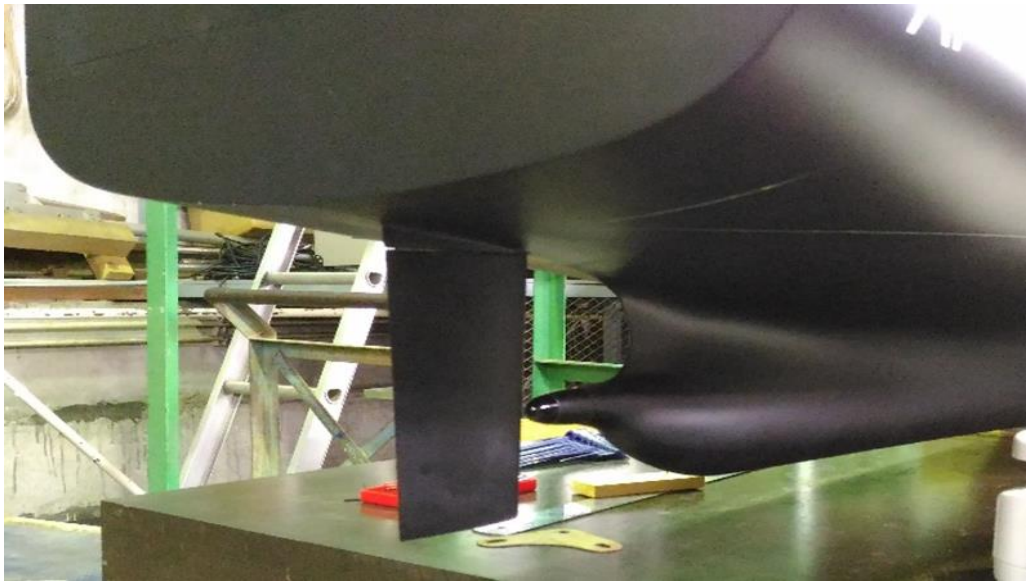

Figure 1: KCS model (bow and stern view)

Table 2: Main particulars of KCS model

Length between perpendiculars: L_{PP} (m)	3.200
Maximum beam of waterline: B (m)	0.448
Depth: D (m)	0.264
Draft: T_D (m); fully loaded condition	0.150
Displacement volume: ∇ (m^3)	0.140
Block coefficient (C_B)	0.651
LCB (%L_{PP}), fwd+	-1.480
Vertical Center of Gravity (from keel): KG (m)	0.199
Radius of gyration (around x axis): K_{XX}	0.4B
Radius of gyration (around y axis): K_{YY}	0.25L_{PP}
Radius of gyration (around z axis): K_{ZZ}	0.25L_{PP}

For the self-propulsion study, a 5-Blade Propeller was installed at a position of 56mm forward of A.P. The main particulars of full-scale propeller are shown in Table 3.

Table 3: Particulars of full-scale propeller

Diameter (m)	7.9
Pitch ratio (P/D) mean	0.95
Section	NACA66
Expanded blade area ratio (ER)	0.80
Rotation direction	Clockwise
Boss ratio	0.18
Number of blades	5

For the model scale ship, model scale propeller has been used for the experiment. The model scale propeller is shown in Figure 2. The main particulars of the propeller model are shown in Table 4. Experiments have been done for λ/L = 0.65, 1.15, 1.37, and in calm water. This propeller is a clockwise rotating propeller. The propeller rotation speed has been determined by EFD self-propulsion test for each wave length. The propeller rotation speed (dimensional and non-dimensional) for different wave length and calm water condition have been shown in Table 5. For the computational study, Osaka University Body Force Propeller Model has been used. Details of this propeller model will be discussed in chapter 4.

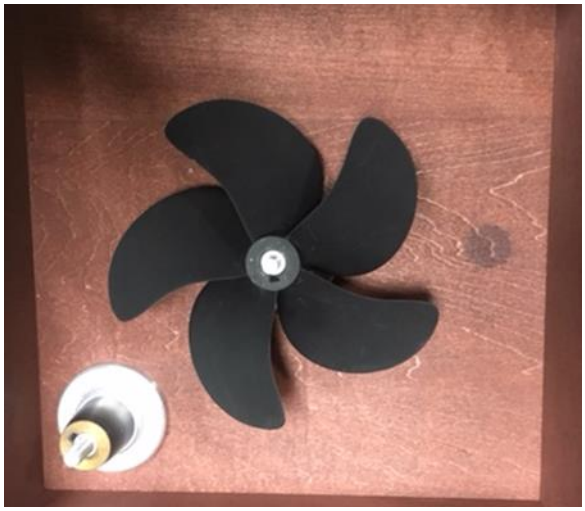

Figure 2: Propeller model for 3.2 m KCS model ship

Table 4: Particulars of propeller model

Diameter (m)	0.1099
Pitch ratio (P/D) mean	0.95
Expanded blade area ratio (ER)	0.80
Boss ratio	0.18
Number of blades	5

Table 5: Propeller rotation speed

λ/L	rps(1/s)	rps(-)
Calm	16.3	35.81
0.65	17.1	37.56
0.85	17.7	38.88
1.15	20.2	44.37
1.37	20.1	44.15
1.95	18.2	39.98

Chapter 3: Experimental Setup

Experiments were conducted in the towing tank of Osaka University. This towing tank has a length of 100m, width of 7.8m and the depth of 4.35m. The wave maker is located at the end of the towing tank and is capable to generate regular and irregular waves. The towing carriage runs between both ends of the tank so motion of ships can easily be observed. Wave absorbers are fitted on both sides of the tank to dampen the waves after each run. The wave maker is capable of generating waves of maximum height 500mm and wavelengths ranging from 0.5 to 15m.

A 3.2m KCS model, corresponding to Reynold's number, $R_e = 4.66\times10^6$ with Froude number, F_n=0.26 (vessel speed = 1.456 m/s), was used for the experiments. Radius of Gyration and VCG was confirmed and adjusted by this swinging equipment (Figure 3). The resistance tests were conducted in waves for the wave-ship length ratio λ/L = 0.65, 0.85, 1.15, 1.37, 1.95 and in calm water. Waves were generated using a plunger type wave maker having 2 motors of 11kW each. The wave meter was installed at the most front of the main carriage. The experimental setup, as shown in Figure 4, was arranged in a way that the ship was free to surge, heave and pitch. At the center of the model ship, a heaving rod was mounted (in a light weight carriage) at which heave, pitch and surge were measured using the potentiometers installed. A servo-type wave height meter was installed in front of the hull (3.005m forward of F.P) to acquire the wave data during the experiment. The forces acting on the X-Direction was measured using the load cell installed on the heaving rod. Pitch free gimbal (Figure 5) under the load cell was attached on the heaving rod end and mounted at the model's center of gravity. The yaw motion was prevented by the yaw guides (Figure 6) installed at both forward and aft of the ship. The thrust/torque dynamometer was installed on the shaft between the motor and propeller. Although the ship is free to surge, it has to be in a same position relative to the towing carriage so that flow field can be measured with SPIV. So, the surge motion needs to be controlled. In the resistance test, the surge motions were controlled by an external force (F_0) generated by the bias loader and a weak spring system for the PIV measurements. In self-propulsion test, by adjusting the propeller revolution, the surge motion was controlled by propeller thrust only. The coordinate system for the experiment is set in a way assuming as 0 when the hull is stationary. X- Coordinate is taken as positive towards the aft of the

ship, Y-Coordinate is taken positive towards starboard direction and positive Z is taken in upward direction. The coordinate system is shown in Figure 7.

Figure 3: Adjustment of the Radius of Gyration

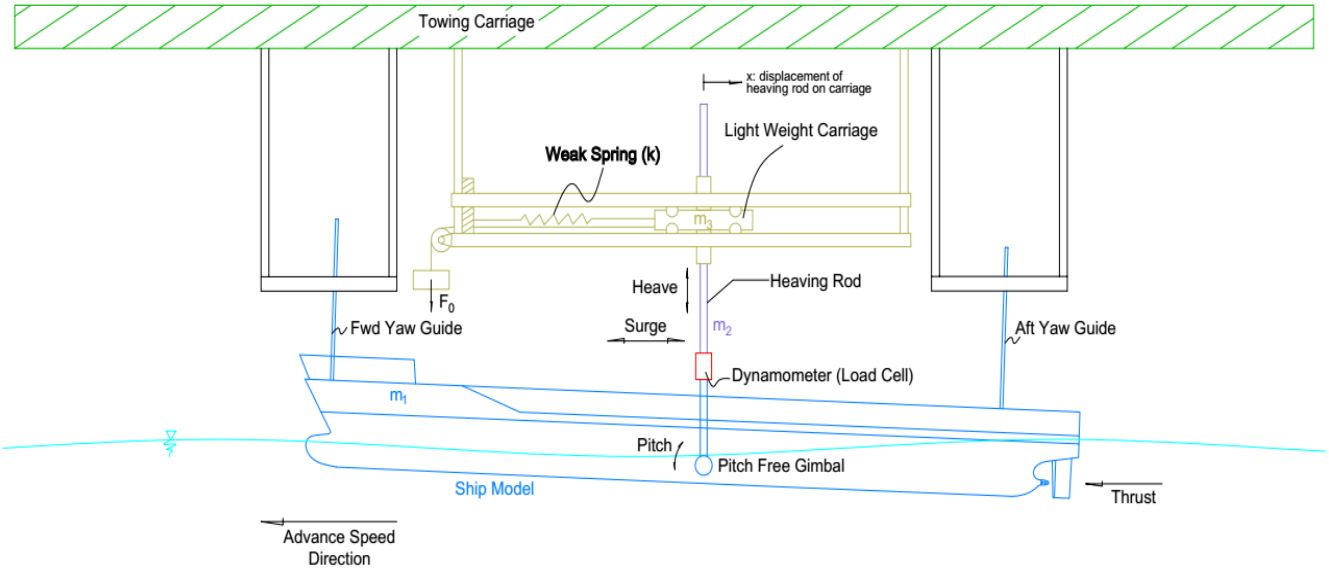

Figure 4: Schematic of Experimental Setup

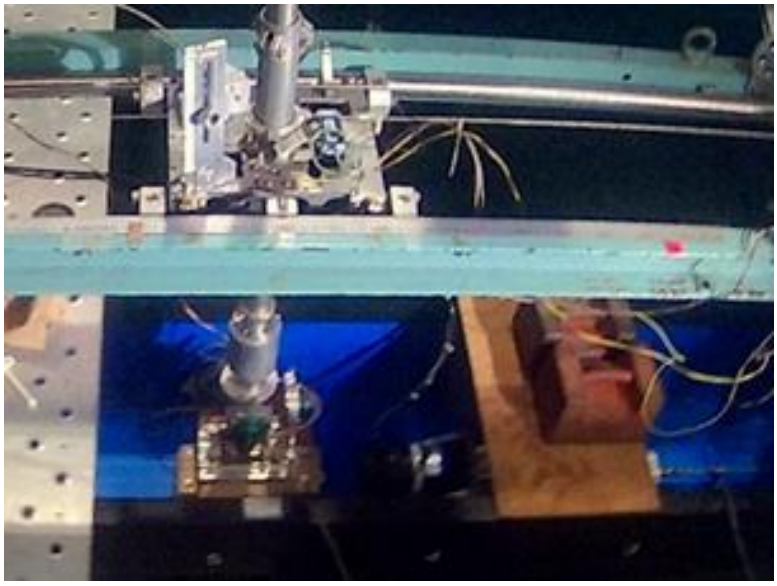

Figure 5: Gimbal

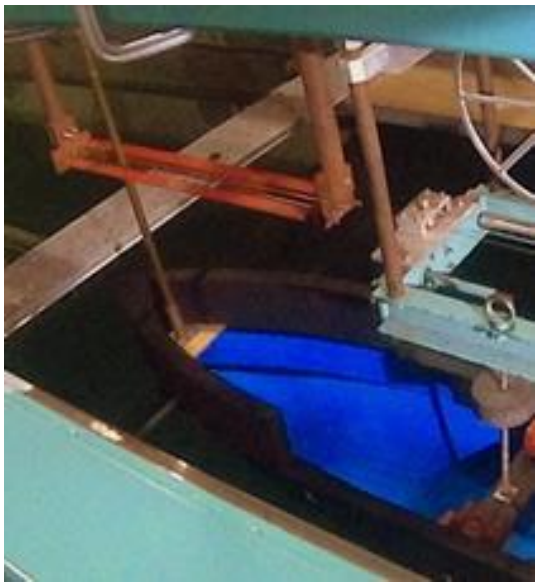

Figure 6: Yaw Guide

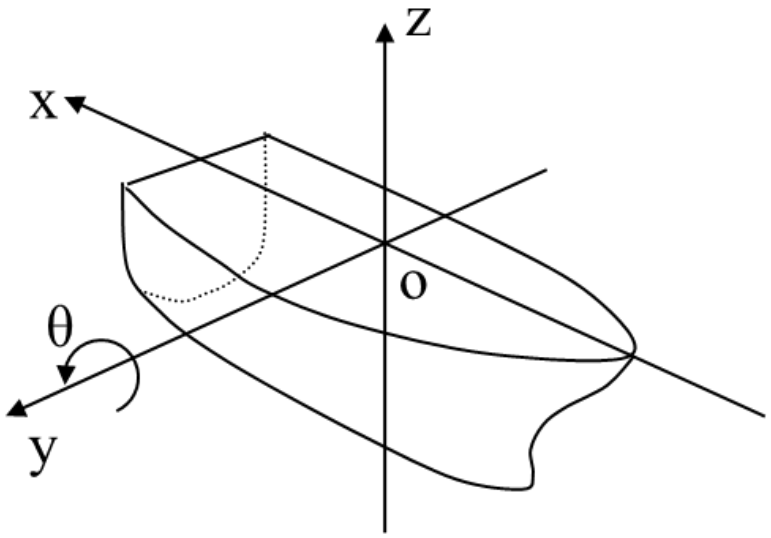

Figure 7: Coordinate system used in experiment

Stereoscopic Particle Image Velocimetry (S-PIV) system, as shown in Figure 8, was utilized to measure the phase averaged velocity flow field at the propeller plane (x/L =0.9825, where x/L =0 at F.P.) for nominal wake as well as several planes before and behind the rudder for self-propulsion condition for λ/L =0.65, 1.15 & 1.37. The wave elevations were obtained at the wave height meter and the output values were passed through the amplifier. Then the amplified signal passed through a built-in AD converter of a computer which was used to synchronize the wave phases and the signal was triggered when the wave crosses the mean value. This trigger signal was used as the reference input to the PIV system's Programmable Timing Unit (PTU). The delay from the triggered signal was adjusted by the PIV system. This way, the wave phases were synchronized and measurement of flow velocities were obtained. The image was captured every 90º phase (i.e. 0.25 of encounter period, T_e) of the cosine waves recorded in wave meter. Approximately 200 images were averaged for each phase of each wave condition.

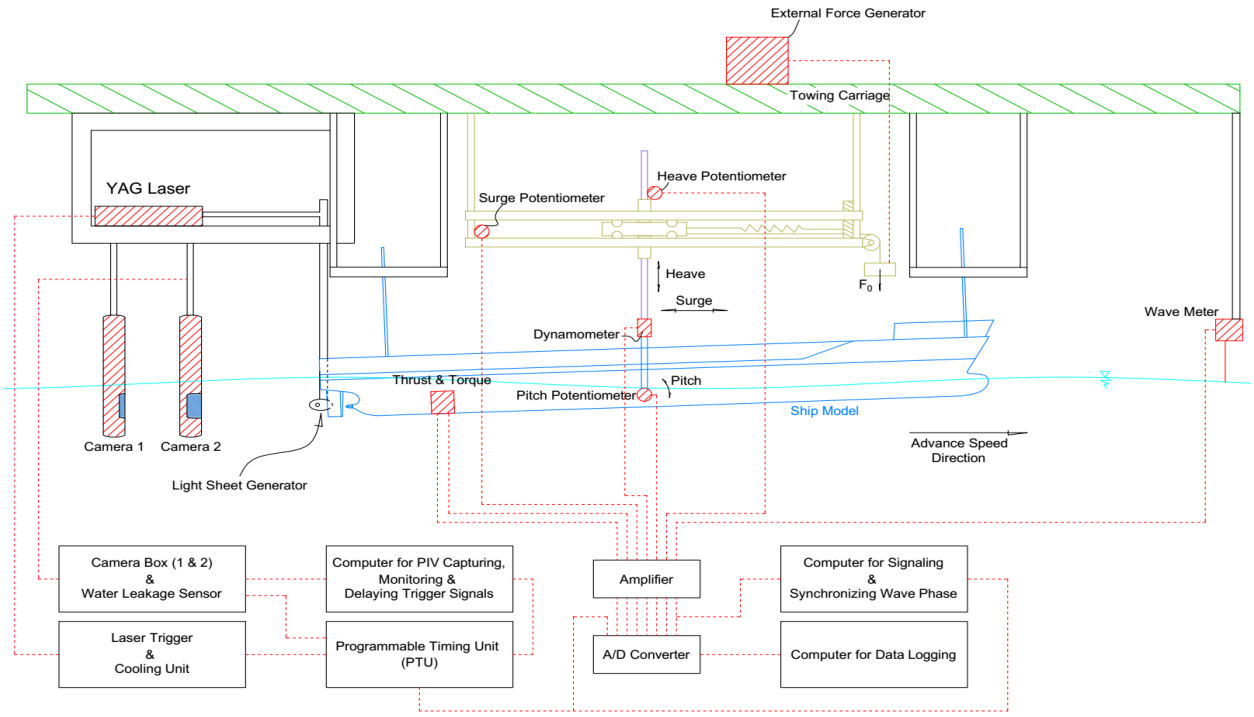

Figure 8: Schematic View of SPIV System

Effect of surge motion on PIV measurement

For usual SPIV measurement, the ship model is fixed rigidly not allowing to surge so that the images can be taken at the intended specified plane. However, there is a risk of breaking of the hull or the heaving rod in this way, as the ship receives very large hydrodynamic forces excited by waves and ship motions. That's why, the present experiments in waves was conducted in the surge free condition as mentioned earlier. Therefore, the resistance obtained from the dynamometer (load cell) would not be the actual hydrodynamic force as the ship model is surging. The actual one has to be processed from the measurement data. From the surge data, the surge velocity and acceleration can also be derived and hence, the hydrodynamic forces can be obtained from the following equations:

$$m_1\ddot{x} + kx = -A \sin \omega_e t \tag{1}$$

$$m_1\ddot{x} = F_x + T - F_H \tag{2}$$

Here,

m_1 = mass of ship model (kg)

$\ddot{x}$ = surge acceleration (m/s^2)

ω_e = encounter wave frequency (1/s)

A = amplitude of surge by encounter wave (m)

F_x = measured force (N) in X-direction at dynamometer (load cell)

T = measured thrust force (N)

F_H = actual hydrodynamic force (N)

Axial flow velocity "u" which is obtained from the SPIV data needs to be corrected as the ship is surging. This can be corrected by using the surge velocities. However, the surge velocities are as low as 0.03 m/sec while the towing speed is 1.456 m/sec. Thus, the influence on the SPIV measurement is not so large and thus, no modifications were made in the present study. CFD and SPIV results both are in tank-fixed coordinate. The SPIV images were capture in the mean surge position.

Table 6: Condition of surge motion in EFD and CFD

	EFD	CFD
Towing Condition	Surge fixed	Surge fixed
Self-propulsion	Controlled surged motion (very small amplitude)	Surge fixed

Chapter 4: Computational Methodology

4.1 Grid Generation

Gridgen V15 - Pointwise software [Pointwise, Gridgen, 2010] has been used for gird generation. Curvilinear structured grids have been used along with multi-block overset grid techniques for the simplification of the grid generation complication. Topological interconnections are used in multi-block techniques to connect the faces of the blocks. This is done using overset techniques, where the interpolation is applied to local cell volumes and faces. The advantage of these interpolation schemes is the applicability to form transient moving grids to account for the relative motions of the ship hull.

In the without propeller condition, the entire grid system is composed of 9 blocks: starboard and portside for hull, cover (hull top), tail/stern (including shaft tube and dummy boss), rudder (attached under transom) and one background. Details of the grids are shown in Table 7. For all the λ/L ratios, the number of grids is same for all the blocks except the Background block, where different grid number has been used for shorter waves (λ/L = 0.65, 0.85) and longer waves (λ/L = 1.15, 1.37, 1.95). The reasons of this difference in grid number will be discussed in the subchapter 4.4 Computational Domain and Boundary Conditions). To capture turbulence, very fine gird (minimum size is approximately 1×10^{-6}) has been used on the solid surface corresponding to y<+1. To capture the free surface deformation in propagating waves, around 20-25 grid points has been distributed per wave amplitude and around 65-195 grid points has been distributed per wavelength. Total number of grids for shorter wave and longer wave are approximately 12.5 million and 12.9 million respectively. The overall grid system (except for the Background block) is shown in Figure 9 along with the coordinate system. For a clear view, Tail and Rudder blocks are shown separately in Figure 10. In this figure, the overset of different blocks can be observed clearly.

For the self-propulsion simulation, a propeller disk has been included. In addition, a small refinement box has been introduced to solve the complication of the overset grids. The propeller disk and the refinement box are shown in Figure 11. Details of the grids are shown in Table 8. The number of grids is same for all the λ/L ratios for self-propulsion condition. Grid point distribution is same as the without propeller condition. Total number of grids is approximately 15.6 million.

Table 7: Details of grids (without propeller)

Block name	λ/L =0.65, 0.85	λ/L =1.15 – 1.95
	$i_{max} \times j_{max} \times k_{max}$	
Hull	206×61×141 ×2	
Cover	206×30×25×2	
Tail	101×41×51×2	
Rudder	43×53×86×2	
Background	216×241×151	226×241×151
Total grid number	12,527438	12,891,248

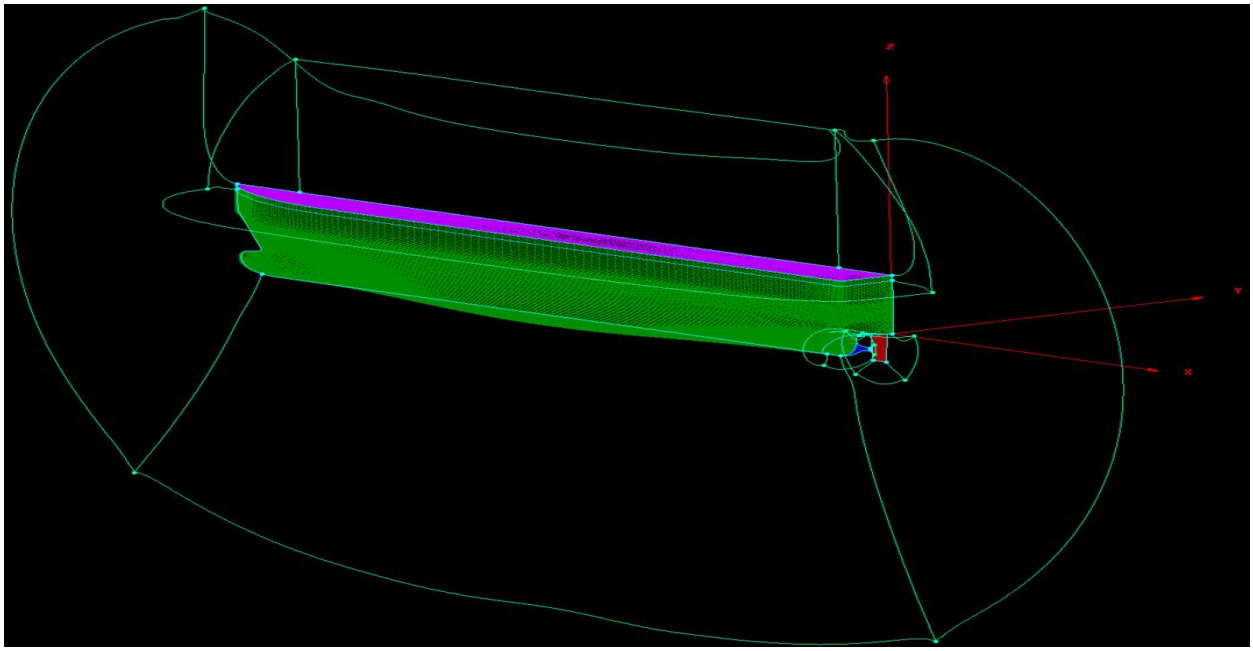

Figure 9: Grid system (without propeller)

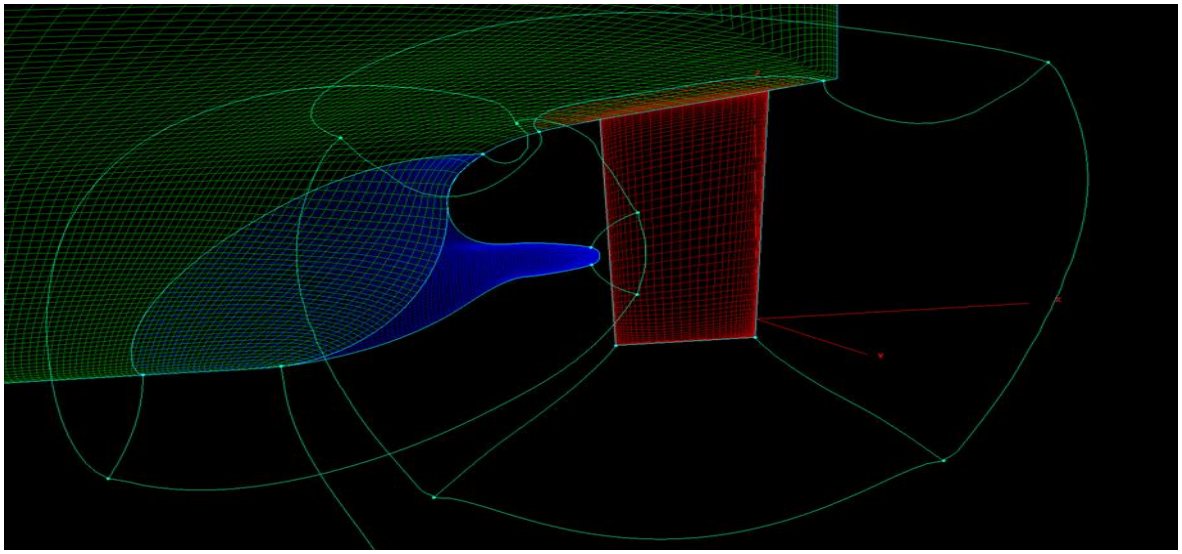

Figure 10: Grids in Tail and Rudder blocks

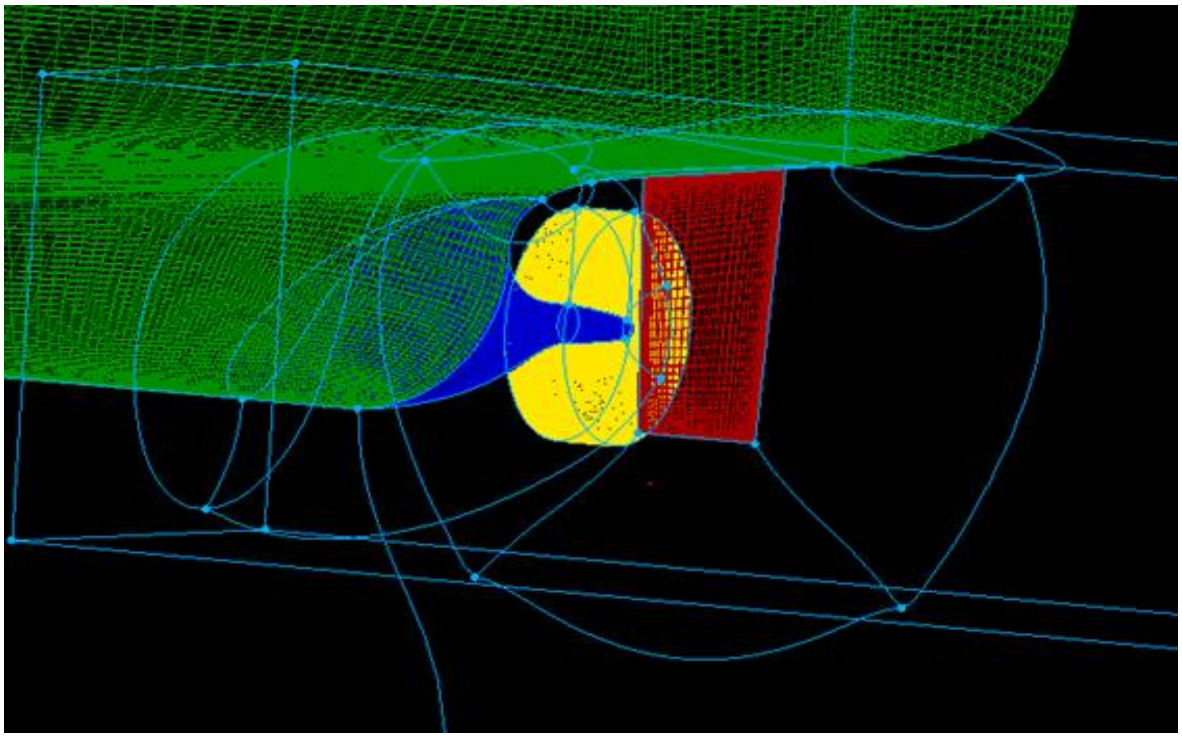

Figure 11: Propeller disk and refinement box

Table 8: Details of grids (propeller included)

Block name	$i_{max} \times j_{max} \times k_{max}$
Hull	206×61×141 ×2
Cover	206×30×25×2
Tail	101×41×51×2
Rudder	43×53×86×2
Propeller disk	35×111×105
Refinement Box	201×81×81
Background	226×241×151
Total grid number	15,594,894

4.2 Overview of CFDShip-IOWA Version 4.5

CFDShip-IOWA Version 4.5 has been used for this CFD validation study. This CFDShip-IOWA code is a block structured, overset and incompressible URANS code coupling with motion solver for ship applications. It has either absolute or relative inertial, non-orthogonal curvilinear coordinate system for arbitrary moving, but non-deforming control volumes. In CFDShip-IOWA, two turbulence models are available: Baldwin-Lomax or the blended k-ω/k-ε (BKW), including an option for shear-stress transport (SST) model [Menter, 1994]. These isotropic and anisotropic RANS and DES approaches include near-wall or no wall functions. Captive, semi-captive, and full 6DOF capabilities for multi-objects with parent/child hierarchy are available in this code. Advanced iterative solvers, higher order finite differences with conservative formulation are included for the numerical analysis. Parallelization feature, with MPI-based domain decomposition, is included as well.

In this study, 2nd order finite difference method has been used for the discretization of the governing equations. The time derivatives in the turbulence and momentum equations has been discretized using second order finite Euler backward difference method. Convection terms in the turbulence and momentum equations has been discretized with higher order upwind scheme. The viscous term in momentum and turbulent equations has been discretized using second order difference scheme. The blended *k*-ω/*k*-ε SST turbulence model was employed using no wall function. A single-phase level-set method has been used to model the free surface and 2DOF (heave and pitch) ship motions are considered. The location of the free surface is given by the 'zero' value of the level-set function, positive in water and negative in air. For the dynamic overset (to obtain the overset interpolation information) of grids of different blocks, SUGGAR library has been used. Two step Projection method has been used for the pressure-velocity coupling. Inertial earth-fixed and non-inertial ship-fixed coordinate systems have been used for solving flow field and ship motions respectively. The detail of equation derivation and numerical approach is in Paterson, et al. (2003), Wilson, et al. (2006), Carrica, et al. (2006), and Xing, et al. (2008). It is a long development history for a CFD code. New numerical techniques were implemented and existed methods were inherited among the code versions.

The grid velocity $\mathbf{u_G}$ caused by ship motions needs to be considered in an incompressible flow field composed of velocity field **u** and pressure field *p*. Thus, the governing equations, i.e. continuity and Reynolds-Averaged Navier-Stokes (RANS) equation are-

$$\nabla \mathbf{u} = 0 \tag{3}$$

$$\frac{\partial \mathbf{u}}{\partial t} + (\mathbf{u} - \mathbf{u_G}) \cdot \nabla \mathbf{u} = -\nabla p + \nabla \cdot \left\{ \frac{1}{R_{e_{eff}}} (\nabla \mathbf{u} + \nabla \mathbf{u}^T) \right\} + \boldsymbol{S} \tag{4}$$

Here,

$\boldsymbol{S}$ = source term

$R_{e_{eff}} = \frac{UL}{\nu + \nu_t}$ = (effective) Reynolds number

$v =$ kinematic viscosity

$v_t =$ kinematic turbulent viscosity/isotropic eddy viscosity

The pressure term is the non-dimensional form of piezometric pressure:

$$p = \frac{p_{abs}}{\rho U^2} + \frac{z}{F_n^2} + \frac{2k}{3} \tag{5}$$

Here,

$p_{abs} =$ absolute pressure

$z =$ depth of water

$F_n = \frac{U}{\sqrt{gL}} =$ Froude number

$g =$ gravitational acceleration

$k =$ turbulent kinetic energy

$L =$ ship length

k and v_t are solved by the SST (shear stress transport) k-ω turbulence model (Menter, 1994).

The grid velocity $\mathbf{u_G}$ is caused by ship 6DOF (degrees of freedom) motions. The ship linear velocities and angular velocities are solved by rigid body equations for the ship rotational center different from its center of gravity (Carrica, et al., 2006):

$$m\{\dot{u} - vr + wq - x_G(q^2 + r^2) + y_G(pq - \dot{r}) + z_G(pr + \dot{q})\} = X \tag{6}$$

$$m\{\dot{v} - wp + ur - y_G(r^2 + p^2) + z_G(qr - \dot{p}) + x_G(qp + \dot{r})\} = Y \tag{7}$$

$$m\{\dot{w} - uq + vp - z_G(p^2 + q^2) + x_G(rp - \dot{q}) + y_G(rq + \dot{p})\} = Z \quad (8)$$

$$I_x\dot{p} + (I_z - I_y)qr + m\{y_G(\dot{w} - uq + vp) + z_G(\dot{v} - wp + ur)\} = K \quad (9)$$

$$I_y\dot{q} + (I_x - I_z)rp + m\{z_G(\dot{u} - vr + wq) + x_G(\dot{w} - uq + vp)\} = M \quad (10)$$

$$I_z\dot{r} + (I_y - I_x)pq + m\{x_G(\dot{v} - wp + ur) + y_G(\dot{u} - vr + wq)\} = N \quad (11)$$

Here,

$m =$ ship mass

$I_x, I_y, I_z =$ moments of inertia respect to the center of rotation

$x_G, y_G, z_G =$ distances between the center of rotation and gravity

$X, Y, Z =$ forces calculated from force integration along the ship hull, propeller and rudder, and then transformed from earth- to ship-fixed coordinates

$K, M, N =$ moments calculated from force integration along the ship hull, propeller and rudder, and then transformed from earth- to ship-fixed coordinates

$u, v, w =$ surge, sway and heave velocities respectively (in ship-fixed coordinates)

$p, q, r =$ roll, pitch and yaw velocities respectively (in ship-fixed coordinates)

The surge, sway, heave, roll, pitch and yaw velocities (u', v', w', p', q', r') in earth-fixed coordinate can be transformed from (u, v, w, p, q, r) and used to compute $\mathbf{u_G}$ (Xing, et al., 2008):

$$\mathbf{u_G} = (u'\hat{\imath} + v'\hat{\jmath} + w'\hat{k}) + (p'\hat{\imath} + q'\hat{\jmath} + r'\hat{k}) \times \boldsymbol{r} \quad (12)$$

Here,

$\boldsymbol{r}$ = instantaneous position vector of the grid point

$\hat{\imath}, \hat{\jmath}, \hat{k}$ = unit vectors in the Cartesian coordinates (x,y,z)

The advantage of using earth- or ship-fixed coordinates to solve ship motions were discussed in Wilson, et al., 2006.

The free surface is modeled by the single-phase level set method (Carrica, et al., 2006). The level set function or distance function φ, defines the free surface along iso-surface $\varphi = 0$, $\varphi > 0$ in water and $\varphi < 0$ in air. φ satisfies the convective transport equation as below-

$$\frac{\partial \varphi}{\partial t} + (\mathbf{u} - \mathbf{u_G}) \cdot \nabla \varphi = 0 \tag{13}$$

To maintain the solution of φ as the distance function to the free surface, the re-initialization procedure is required (Carrica, et al., 2006). It ensures the change rate of current solution φ in normal direction n follows the previous solution φ_0:

$$\frac{\partial \varphi}{\partial n} = sign(\varphi_0) \tag{14}$$

In order to solve the equations numerically, at first the physical domain in Cartesian coordinates (x, y, z, t) including spatial and temporal terms are transformed into the computational domain in nonorthogonal, curvilinear and non-dimensional coordinates (ξ, η, ς, τ). To solve Eq. (4) and (14), the 2nd order Euler backward differences are used for the temporal discretization of all variables. For an arbitrary variable φ-

$$\frac{\partial \varphi}{\partial t} = \frac{1}{\Delta \tau} \left(\frac{3}{2} \varphi^n - 2\varphi^{n-1} + \frac{1}{2} \varphi^{n-2} \right) \tag{15}$$

where n is the time step and τ is the time in computational domain. The rigid body motion equations Eq. (6-11) is solved numerically by a predictor-corrector method. It is a 2nd order method (Carrica, et al., 2006). For any of the degrees of freedom φ, the predictor step is explicit which solves-

$$\dot{\varphi}^n = \dot{\varphi}^{n-1} + \frac{1}{2}\Delta\tau(\ddot{\varphi}^{n-1} + \ddot{\varphi}^{n-2}) \tag{16}$$

$$\varphi^n = \varphi^{n-1} + \frac{1}{2}\Delta\tau(\dot{\varphi}^{n-1} + \dot{\varphi}^{n-2}) \tag{17}$$

The corrector step is implicit which solves:

$$\dot{\varphi}^n = \dot{\varphi}^{n-1} + \frac{1}{2}\Delta\tau(\ddot{\varphi}^{n} + \ddot{\varphi}^{n-1}) \tag{18}$$

$$\varphi^n = \varphi^{n-1} + \frac{1}{2}\Delta\tau(\dot{\varphi}^{n} + \dot{\varphi}^{n-1}) \tag{19}$$

The spatial discretization for the convective terms is the 2nd order upwind method (Paterson, et al., 2003). For an arbitrary variable φ-

$$U^i\frac{\partial\varphi}{\partial\xi_i} = \frac{U^i+|U^i|}{2}\left(\frac{1}{2}\varphi_{i-2} - 2\varphi_{i-1} + \frac{3}{2}\varphi_i\right) + \frac{U^i-|U^i|}{2}\left(-\frac{3}{2}\varphi_i + 2\varphi_{i+1} - \frac{1}{2}\varphi_{i+2}\right) \tag{20}$$

The viscous/diffusion terms are solved by the 2nd order central difference method (Paterson, et al., 2003). For an arbitrary variable φ-

$$\frac{\partial^2\varphi}{\partial\xi_i\partial\xi_i} = \varphi_{i-1} - 2\varphi_i + \varphi_{i+1} \tag{21}$$

In both Eq. (20) and (21), ξ_i for i=1, 2, and 3 represents the curvilinear coordinates (ξ, η, ς) for the three directions respectively. U^i is the fluid velocity.

4.3 Propeller Model

For the self-propulsion study, the Osaka University Body Force Propeller Model (Yokota, 2013) has been used. A separate subroutine has been used, which is incorporated with CFDShip-IOWA. A simplified quasi-steady blade element theory with the infinite-bladed propeller model (time averaged propeller induced velocity field) is coupled with a RANS code to determine the thrust and the torque distributions. The model aims to reduce the computational effort while keeping the effect of ship with motion in quasi-steady manner for propeller.

Blade element theory was established as a computational tool to predict the propeller performance using the CFD output velocity components at propeller plane. It is based on the assumption that each element of a propeller can be considered as an airfoil segment. The propeller blade with radius R, is divided into equal sections in radial direction. Velocities and forces acting on a blade element are shown in Figure 12.

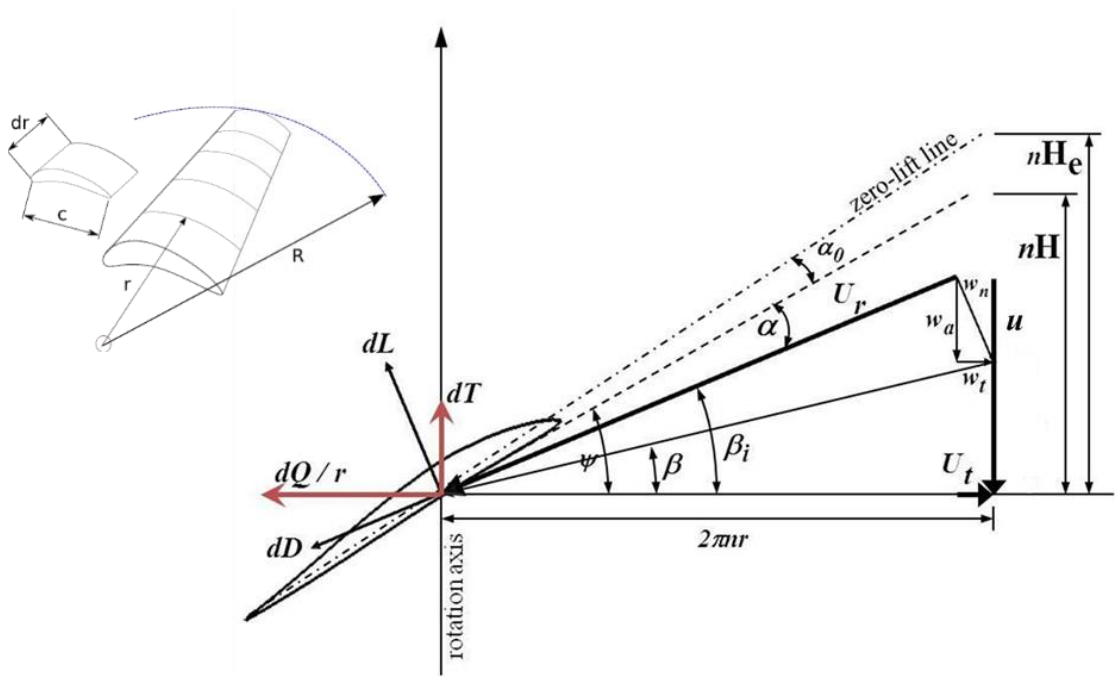

Figure 12: Velocity triangles and forces acting on a blade element

The lift (L) and drag (D) forces are calculated from the resultant velocity, which is expressed by Eq. (22), acting on the airfoil. The variables in the following equations and figures are non-dimensionalized by propeller radius R, free stream velocity U_0 and the water density ρ.

$$U_r = \sqrt{u^2 + (2\pi nr - U_t)^2} \tag{22}$$

Here,

$u =$ axial velocity including induced velocity in CFD code

$U_t =$ tangential velocity including induced velocity in CFD code

$n =$ number of revolutions of the propeller

The total induced velocity is -

$$w_n = \sqrt{{w_a}^2 + {w_t}^2} \tag{23}$$

Here,

$w_a =$ axial induced velocity

$w_t =$ tangential induced velocity

Other governing equations are as follows-

$$Hydrodynamic\ pitch\ angle,\ \beta_i = \arctan\left(\frac{u}{2\pi nr - U_t}\right) \tag{24}$$

$$Lift\ coefficient, C_L = 2\pi k_1 \sin(\alpha + \alpha_0) \tag{25}$$

$$k_1 = 1.07 - 1.05\left\{\frac{c(r_e)}{R}\right\} + 0.375\left\{\frac{c(r_e)}{R}\right\}^2 \quad (r_e = 0.7r) \tag{26}$$

$$Drag\ coefficient, C_D = 0.04348 \tag{27}$$

$$\mathrm{dL} = \frac{1}{2} C_L {U_r}^2 c(r) \tag{28}$$

$$\mathrm{dD} = \frac{1}{2} C_D {U_r}^2 c(r) \tag{29}$$

$$\mathrm{dT} = \mathrm{dL}\cos\beta_i - dD sin\beta_i \tag{30}$$

$$\mathrm{dQ} = (\mathrm{dL}\sin\beta_i - dD cos\beta_i) r \tag{31}$$

$$fb_x = \frac{dT}{\Delta x}\frac{N}{2\pi r} \tag{32}$$

$$fb_\theta = \frac{dQ}{\Delta x}\frac{N}{2\pi r^2} \tag{33}$$

$$T = \int_0^{2\pi}\int_{R_B}^{R} fb_x \Delta x r dr d\theta \tag{34}$$

$$Q = \int_0^{2\pi}\int_{R_B}^{R} fb_\theta \Delta x r^2 dr d\theta \tag{35}$$

Here, Δx is the grid spacing in axial direction at body-force point N represents the number of blades.

Two-dimensional sectional lift coefficient of the propeller blade is calculated using Eq. (25) by taking into account the effect of blade to blade interaction. This effect is included as a correction factor k_1, which is calculated by Eq. (26) (Yamazaki, 1977). Moreover, two-dimensional sectional drag coefficient of the propeller blade is assumed to be 0.04348. The effective pitch (He) is taken as 1.08 times of the geometric pitch of the propeller (H). Finally, the body-forces acting in radial and angular direction on the propeller plane are computed by Eq. (32) and (33), respectively. The overall thrust (T) and torque (Q) of the are obtained by integrating the individual contribution of each element, shown in Eq. (30) and Eq. (31), along the radius of the propeller using Eq. (34) and Eq. (35).

4.4 Computational Domain and Boundary Conditions

In CFD Ship-IOWA, the ship length is 1 (non-dimensionalized) and the origin (0, 0, 0) in the 3D Cartesian coordinate system is set at the forward perpendicular (FP). The ship length is along the X-axis, so the aft perpendicular (AP) is located at (1, 0, 0). The Y-axis is positive to the starboard side and the Z-axis is positive upward. The free surface is placed on z = 0 plane. All the predicted motion responses, obtained in the output files, correspond to the response at the FP (0, 0, 0) of the ship.

The computational domain is different for short waves (λ/L =0.65, 0.85) and long waves (λ/L =1.15, 1.37 1.95). The computational domain is $-0.5 \leq x \leq 1.35, -1 \leq y \leq 1$ and $-1 \leq z \leq 0.22$ for short waves; whereas the it is $-0.6 \leq x \leq 1.35, -1 \leq y \leq 1$ and $-1 \leq z \leq 0.22$ for long waves. The reason for having longer computational domain for long waves is the numerical bounce of the solution. We found that if the upstream length is kept same as that of the short waves (x=*-0.5*), the ship motions would be over-predicted. It might be caused by, the reflected long waves bounce back from the inlet numerically, as it is closer to the bow of the ship. To avoid this problem, the upstream length has been extended (to x=*-0.6*). The computational domain is shown along with the imposed boundary conditions in Figure 13. Incident waves were generated at the domain inlet.

Different types of boundary conditions have been applied on different surfaces. Wave boundary condition and exit boundary conditions have been applied at the inlet and outlet of the background box respectively. The wave boundary condition includes linear propagating wave of cosine

function. On both sides along Y-axis ($y = 1$ and,$y = -1$), zero gradient boundary condition has been imposed. Far field boundary conditions have been applied on the top and bottom of the computational domain. No slip boundary condition has been applied on the ship solid surface.

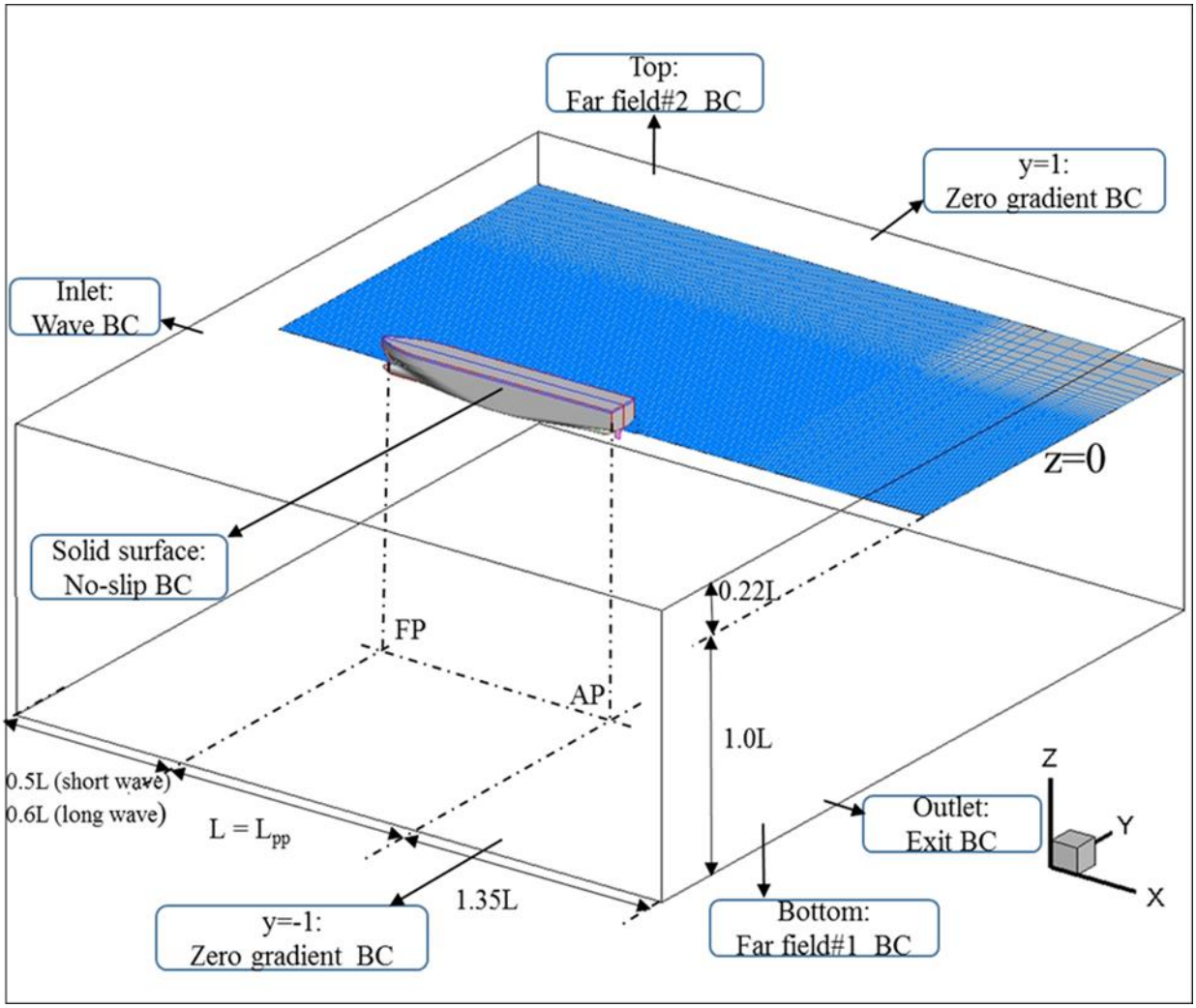

Figure 13 Computational domain along with the boundary conditions

The features of the different boundary conditions have been summarized and shown in Table 9. Equations (36 - 39) has been used to describe the Inlet boundary condition-

$$\zeta(x_0, t) = A\cos(kx_0 - \omega_e t) \tag{36}$$

$$u(x_0, z, t) = \omega A e^{kz}\cos(kx_0 - \omega_e t) + U_0 \tag{37}$$

$$w(x_0, z, t) = \omega A e^{kz}\sin(kx_0 - \omega_e t) \tag{38}$$

$$\hat{p}(x_0, z, t) = \frac{\omega^2 A e^{kz}}{k}\cos(kx_0 - \omega_e t) - \frac{\omega^2 A^2 e^{2kz}}{2} \tag{39}$$

Here,

$\zeta =$ Unsteady free surface elevation,

$A =$ Wave amplitude

$k = \frac{2\pi}{\lambda} =$ Wave number

$\omega =$ Wave frequency

$\omega_e =$ Encounter frequency

$x_0 =$ Location of inlet in X-direction

Table 9: Boundary conditions

Type	Location	U	V	W	$\hat{p}$	k_t	ω_t	ν_t	ζ
Wave	Inlet	*Eq. (37)*	*0*	*Eq. (38)*	*Eq. (39)*	*0*	*0*	*0*	*Eq. (36)*
Exit	Outlet	$\partial^2 U=0$	$\partial^2 V=0$	$\partial^2 W=0$	$\partial\hat{p}=0$	$\partial k_t=0$	$\partial\omega_t=0$	$\partial\nu_t=0$	*0*
Zero gradient	Two sides of background (y=1 and y=-1)	$\partial U=0$	$\partial V=0$	$\partial W=0$	$\partial\hat{p}=0$	$\partial k_t=0$	$\partial\omega_t=0$	$\partial\nu_t=0$	*0*
Far field #1	Bottom of background	U_0	$\partial V=0$	$\partial W=0$	*0*	$\partial k_t=0$	$\partial\omega_t=0$	$\partial\nu_t=0$	*0*
Far field #2	Top of background	U_0	*0*	*0*	$\partial\hat{p}=0$	$\partial k_t=0$	$\partial\omega_t=0$	$\partial\nu_t=0$	*0*
No-slip	Ship's solid surfaces	*0*	*0*	*0*	$\partial\hat{p}=0$	*0*	$\frac{60}{Re\beta\Delta y^2}$	*0*	*0*

Chapter 5: Results and Discussions

5.1 Ship Motions

At first, the simulation results have been validated for heave and pitch motions. In CFDShip-IOWA, computation and time-history output, the motion responses are relative to ship C.G. (center of gravity) corresponding to wave crest at FP. On the other hand, the EFD measurements were done at the wave gauge meter. Therefore, the data of EFD measurements have been shifted to the FP from the wave gauge meter for the comparison with the predicted CFD results. The time history comparison of CFD and EFD wave, heave and pitch motions for λ/L =1.15 have been shown in Figure 14. The wave at FP and the heave motions are shown in centimeter (cm) whereas the pitch motions are represented in degree. The time history comparison for the ship motions show a little phase lag (Motion phase difference is around 0.06-0.07 sec).

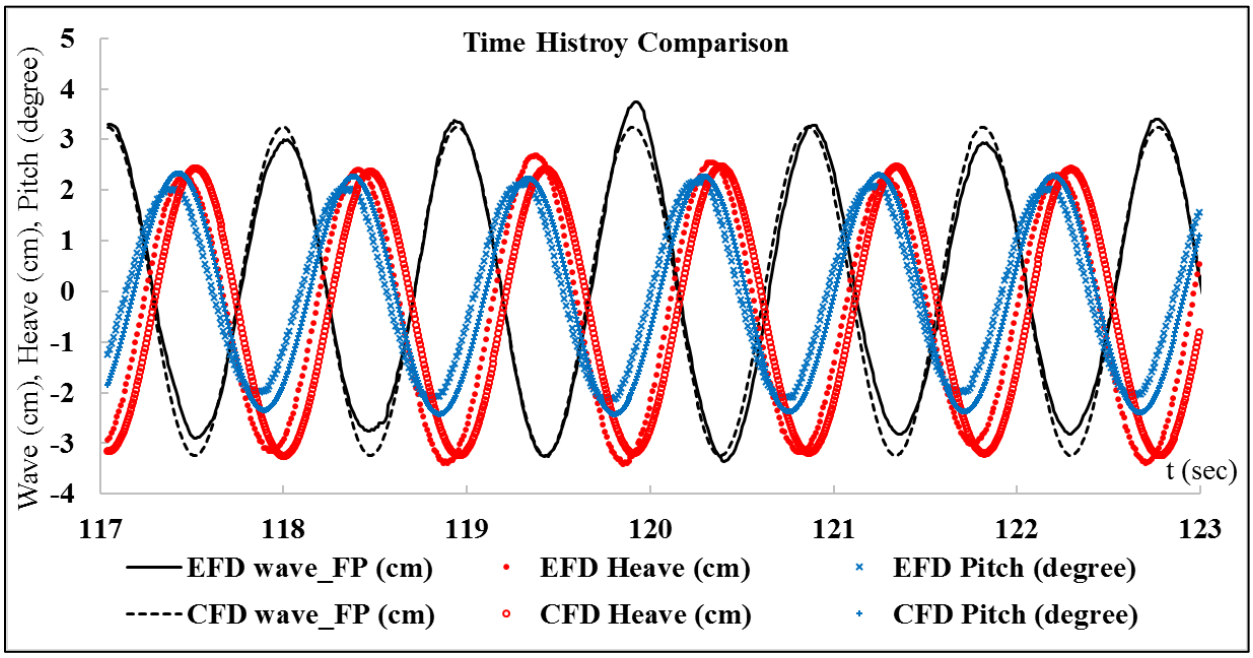

Figure 14 Time history comparison of CFD and EFD wave, heave and pitch motions for λ/L =1.15

The origin of the difference can be traced back to both CFD and EFD. It requires very comprehensive and further study. In CFD, the spatial and temporal discretization, i.e. the

combination of grid size Δx and time step Δt, are very hard to capture wave crest or trough at the exact place and time. Constant non-dimensional Δt=0.025 was used for all wave lengths. The time step number N_e has to be an integer number in one wave encounter period T_e but T_e divided by Δt is not an integer number. For example, the non-dimensional T_e for λ/L =1.15 is 0.434708, so N_e =174 plus or minus one or two. The same situation was observed for Δx. Although the grid size was designed carefully as mentioned in the previous chapter, it is very hard to keep an integer grid number per wave length and height. Especially, the grid topology around the ship model is O- or double C-grid. Also, there is an overset region between the ship body and background block.

For EFD, although the wave meter was mounted in the most front end of the carriage, not only the probe needle was disturbing the wave incoming toward the ship but also the distance between the wave meter and ship center of gravity (or FP) was very hard to measure because of the towing tank structure. Also, as seen in Figure 14, the wave quality will need to be improved, i.e. wave maker maintenance. The wave amplitude and phase were varying slightly.

The CFD code provides the heave and pitch motion responses in the time domain. For all wave conditions, as outlined in Chapter 2: Objective and Conditions, the convergence of the motions is found after 5,000 iterations, whereas 10,000 are needed for the convergence of the result for calm water. Heave and pitch motions have been calculated for all wave conditions and in calm water as well. A converged region for heave and pitch data has been chosen for the Fourier Transformation. A simple FORTRAN code has been made for this Fourier Transformation. Predicted motions responses have been used as the input for this Fourier Transformation. It was shown in [Sadat-Hosseini et al., 2015] that the 1st harmonic motions are the most influential parts. Non-dimensional 1st harmonic heave amplitude has been compared with different EFD results for a wide range of λ/L , as shown in Figure 15. The heave amplitude has been non-dimensionalized by the wave amplitude, A. The predicted heave amplitude shows good agreement with the EFD results.

Non-dimensional 1st harmonic pitch amplitude has been compared with different EFD results for a wide range of λ/L , as shown in Figure 16. The pitch amplitude has been non-dimensionalized by the wave slope, Ak. The predicted pitch amplitude agrees well with the EFD results.

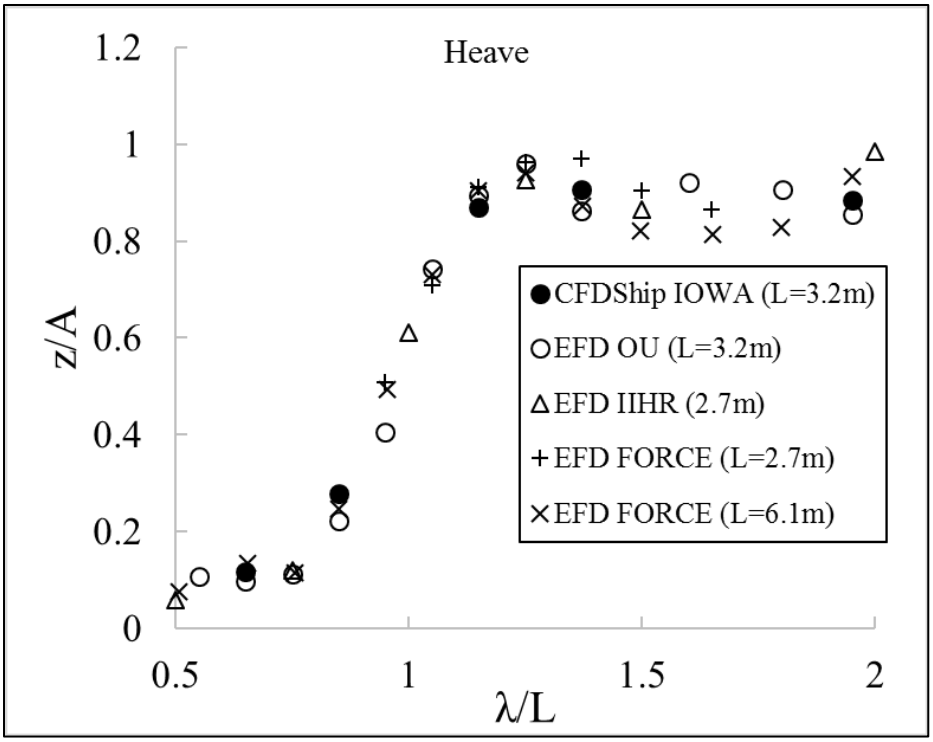

Figure 15 1st harmonic heave motion amplitude (non-dimensional)

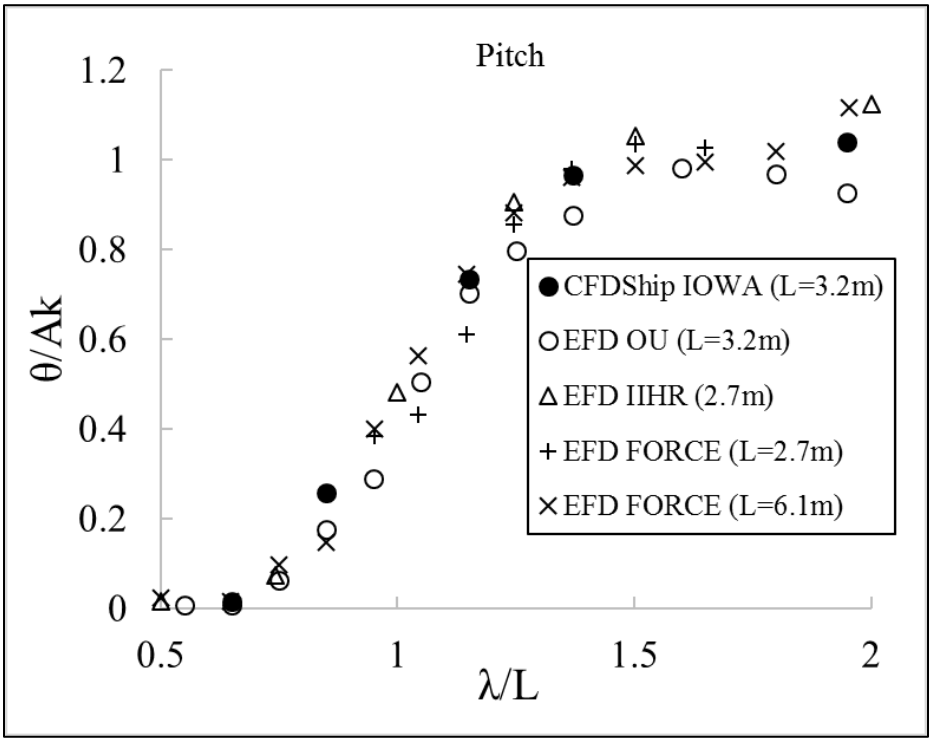

Figure 16 1st harmonic pitch motion amplitude (non-dimensional)

In short waves, typically for λ/L <0.5, z/A and θ/Ak are near zero indicating very small vertical motions. This is almost similar to the calm water scenario. With the increase of λ/L, vertical motions are increased. In long waves, especially for λ/L >1.15, z/A and θ/Ak both are close to one which indicates the ship moves up vertically as the wave amplitude and the pitch angle follows the wave slope.

5.2 Added Resistance

Calm water resistance has been calculated first from the force output data. Then the resistance in wave conditions have been computed in similar manner. The difference between the resistance in wave and the resistance in calm water is the added resistance. Again, the converged region has been chosen and Fourier Transformation has been performed. The average value has been used for the comparison. This calculated added resistance is in Newton (N). This added resistance has been non-dimensionalized and the added resistance coefficient has been calculated using the following formula-

$$\sigma_{AW} = \frac{R_{AW}}{g\rho A^2 (B^2/L)} \tag{40}$$

The added resistance coefficient, σ_{AW} has been compared with the EFD measurement of Osaka University as well as of other institutions for a wide range of λ/L , as shown in Figure 17. In short waves, typically λ/L <0.5, σ_{AW} is very small and is due to the wave diffraction hitting the ship bow. With the increase of λ/L , vertical motions increase and consequently σ_{AW} increases until it reach to the peak value at λ/L =1.15. In long waves, especially λ/L >1.15, since both heave and pitch motion amplitudes are close to one which indicates the ship moves up vertically as the wave amplitude and the pitch angle follows the wave slope, hence σ_{AW} drops down gradually. The predicted results of added resistance coefficient show fair agreement with that of the EFD measurements of different institutions [Sadat-Hosseini, 2015]. An obvious σ_{AW} deviation between CFD and EFD (except for EFD FORCE [L=2.7m]) can be seen at λ/L =1.37, where the θ/Ak was over-predicted as well.

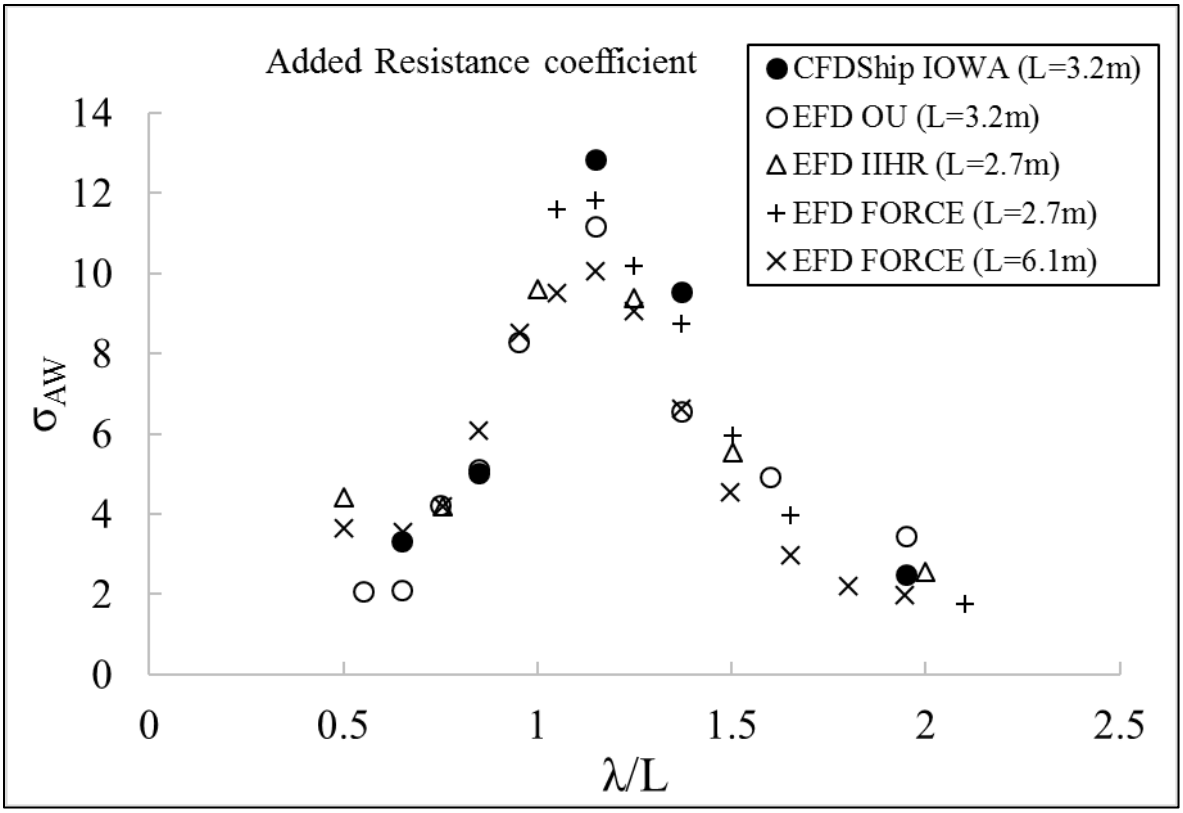

Figure 17 Added resistance coefficient

5.3 Nominal Wake

5.3.1 Nominal Wake in Calm Water

Computed nominal wake at the propeller plane (x/L =0.98) in calm water has been compared with that of EFD in Figure 18. Velocity distribution and the boundary layer profile are observed a little bit different between EFD and CFD. The reason is although it is the calm water case; there is a very small elevation variation of the free surface. Therefore, the ship has very small vertical motions and the convergence requires a huge iteration time stem, i.e. longer computational time. Due to this small oscillation about a certain averaged value (sinkage and trim), the CFD result is slightly different from the EFD one.

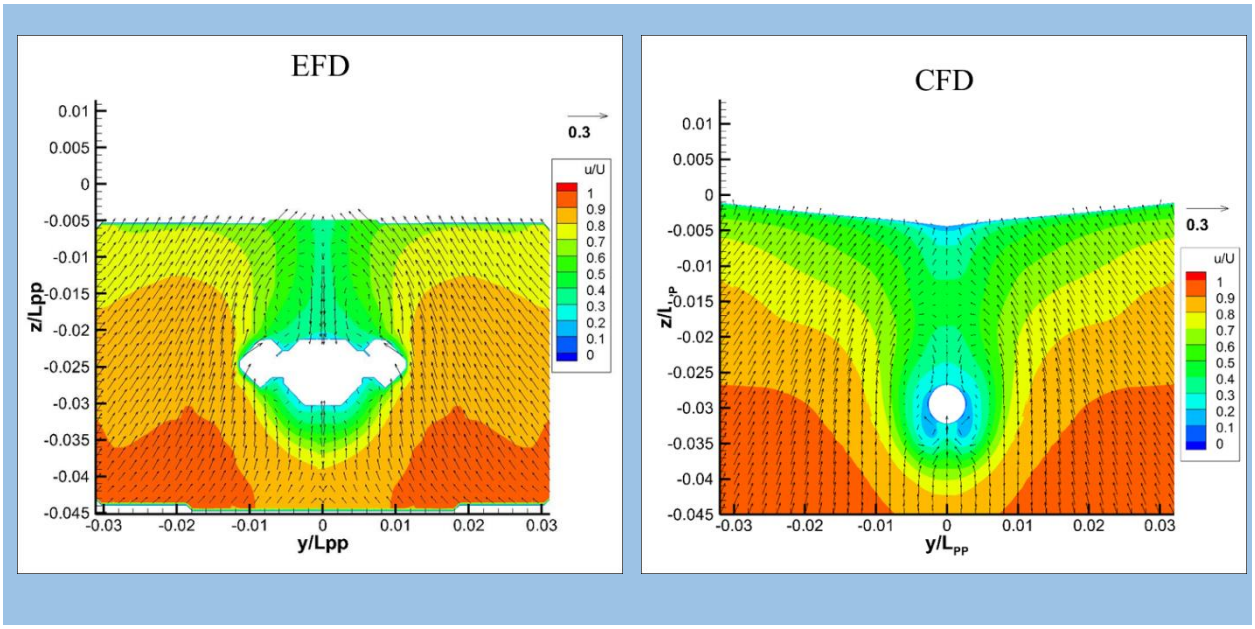

Figure 18 Nominal wake in calm water

The bilge vortex located above the boss and in the upper region of propeller area (r_P/L_{PP}=0.0172) around propeller radius r/r_P=0.3~0.6. It is in the medium layer of the ship boundary layer, i.e. u/U=0.3~0.6. CFD and S-PIV results show the bilge vortex is in the region of r/r_P=0.3~0.6, u/U=0.3~0.6, and -0.008<y/L_{PP} <-0.002 above the dummy boss. However, compared to S-PIV, the bilge vortex in CFD is in lower z/L_{PP} location. Inside the bilge vortex, the shortest vector in CFD is around z/L_{PP}=-0.025; in S-PIV it is around -0.017. The deviation is due to the error of the trim. The secondary vortex under the boss is in the lower portion of propeller area inside r/r_P=0.3. It is induced inside a low speed area u/U<0.3 and clearly observed in CFD. However, in S-PIV result, it is mostly blocked by the blank region caused by laser reflection problem. Only a small portion of light blue area (u/U=0.2~0.3) with some vectors can be seen around z/L_{PP}=-0.03 and -0.004<y/L_{PP} <-0.002. Both vortices are observed inside ship boundary layer and propeller radius. In the outer region, stern upward flow is found.

5.3.2 Nominal Wake in Waves

After the validation of the nominal wake in calm water, the study has been concentrated to validate the CFD code for the nominal wake in different wave conditions. As outlined earlier, in CFDShip-IOWA, all the simulations results for in the output file are correspond to the result at FP; but we

are interested at the propeller plane this time. Therefore, the wave at the FP is shifted to the propeller plane (x/*L* =0.98). Wave at FP, wave at propeller plane, heave and pitch motions for at λ/L =1.15 one-encounter period have been shown in Figure 19. t/Te =0, when the wave crest is at bow (FP). Four time instances (t/Te), for λ/L = 1.15, are shown in this figure with vertical lines. 0°, 90°, 180° and 270° are the wave phases at the wave gauge measured during PIV experiment. CFD and EFD nominal wake data have been compared at these quarter time steps.

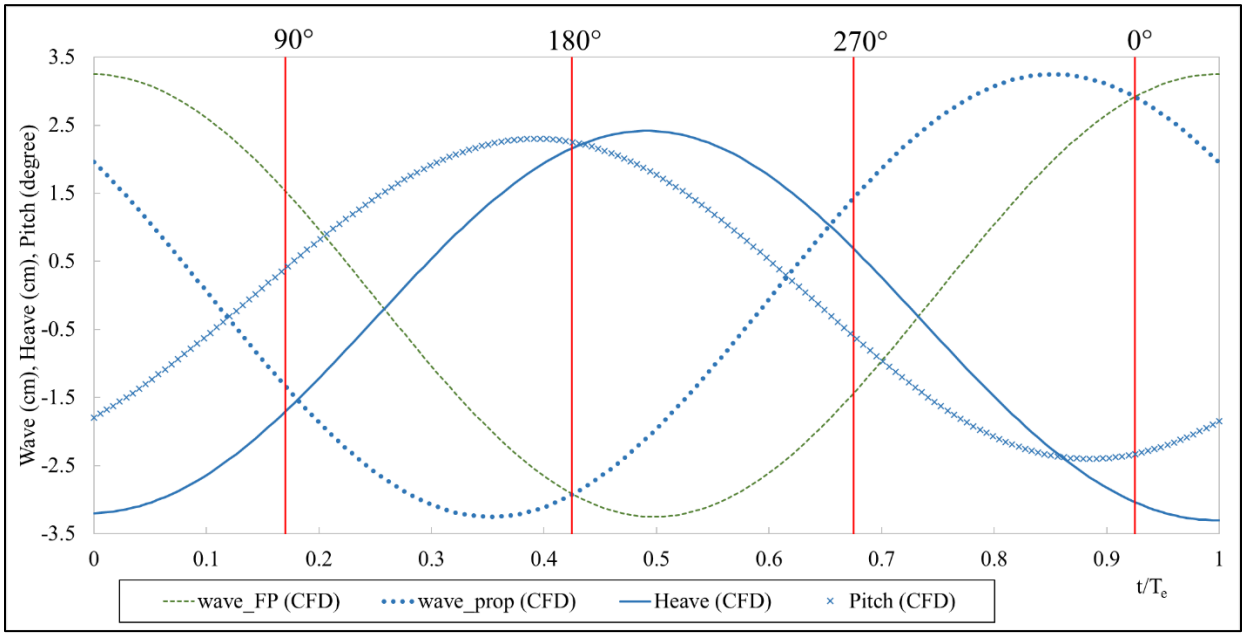

Figure 19 Time history of CFD wave (at FP and propeller plane), heave and pitch motions at λ/L =1.15 for one period, along with the indication of time for the EFD measurements

Since the peak value of the added resistance coefficient appears at λ/L =1.15, it is important to validate the nominal wake results for this wave condition first. Comparison of EFD and CFD nominal wake at λ/L =1.15 (0 degree) is shown in Figure 20. At this moment (t/Te = 0.925), the ship stern just starts to move downward and the low speed area (in light blue shedding) can be observed above the propeller dummy boss. The outer boundary layer is visible. It mainly consists of free stream and wave orbital velocity, and would suppress the inner boundary layer thickness to become narrower in y-direction. Note that, CFD simulations were conducted with surge fixed condition and the SPIV images were captured in the mean surge position.

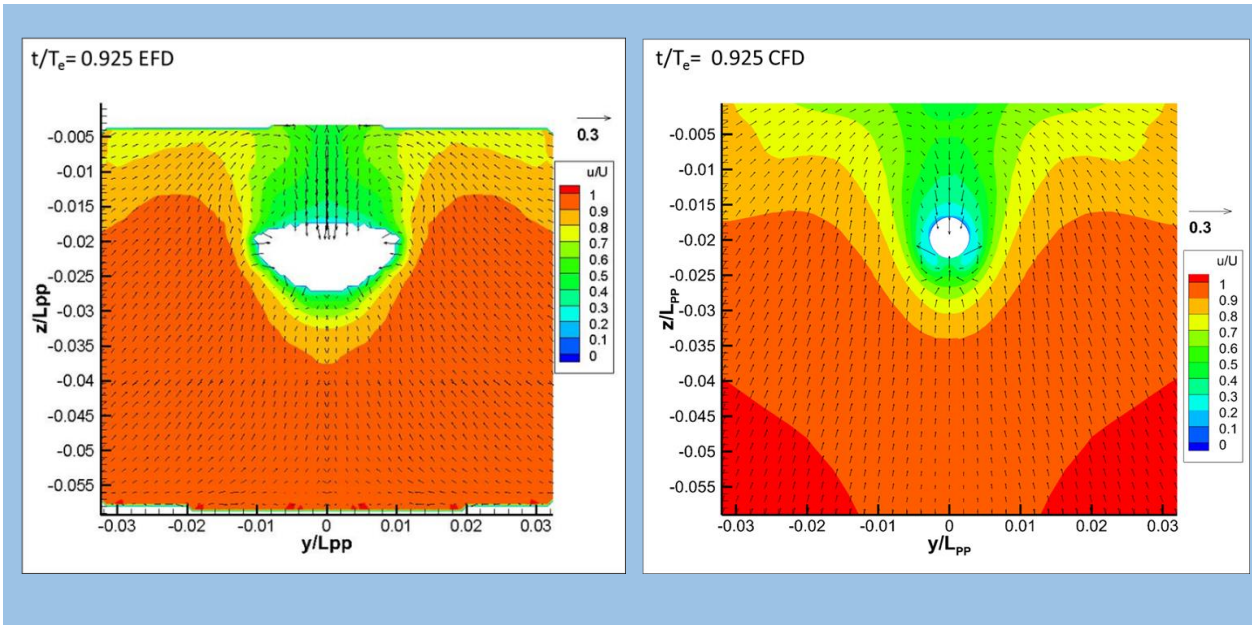

Figure 20 Comparison of EFD and CFD nominal wake at λ/L =1.15 (0 degree)

Comparison of EFD and CFD nominal wake at *λ/L* =1.15 (90 degree) is shown in Figure 21. At this moment (t/ Te~0.17), the ship stern goes downward which can be easily understood by the low speed area (in blue color shedding) above the dummy boss. The bilge vortex can be observed on the sides of the dummy boss although the secondary vortex is suppressed under the boss.

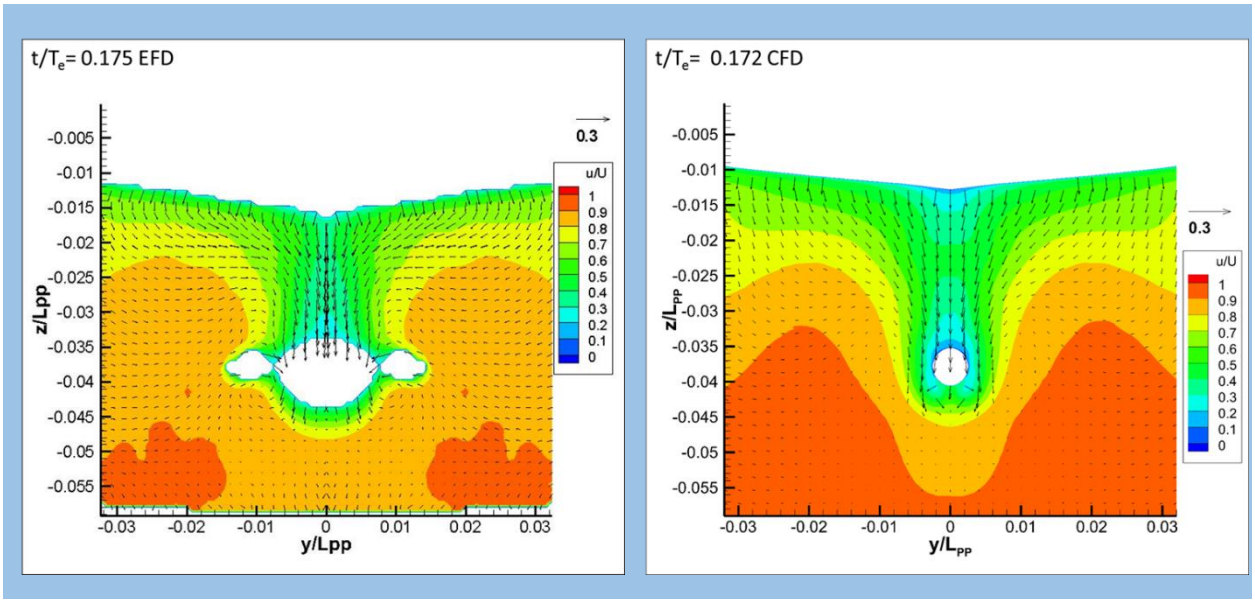

Figure 21 Comparison of EFD and CFD nominal wake at λ/L =1.15 (90 degree)

Comparison of EFD and CFD nominal wake at λ/L =1.15 (180 degree) is shown in Figure 22. When t/Te = 0.425, the ship stern starts to move upward and thus the low speed area under the boss outspreads downward. The secondary vortex is clearly noticeable this time. The bilge vortex is found just above the boss. The velocity distribution, boundary layer and the vortex predicted by CFD shows good agreement with the EFD results.

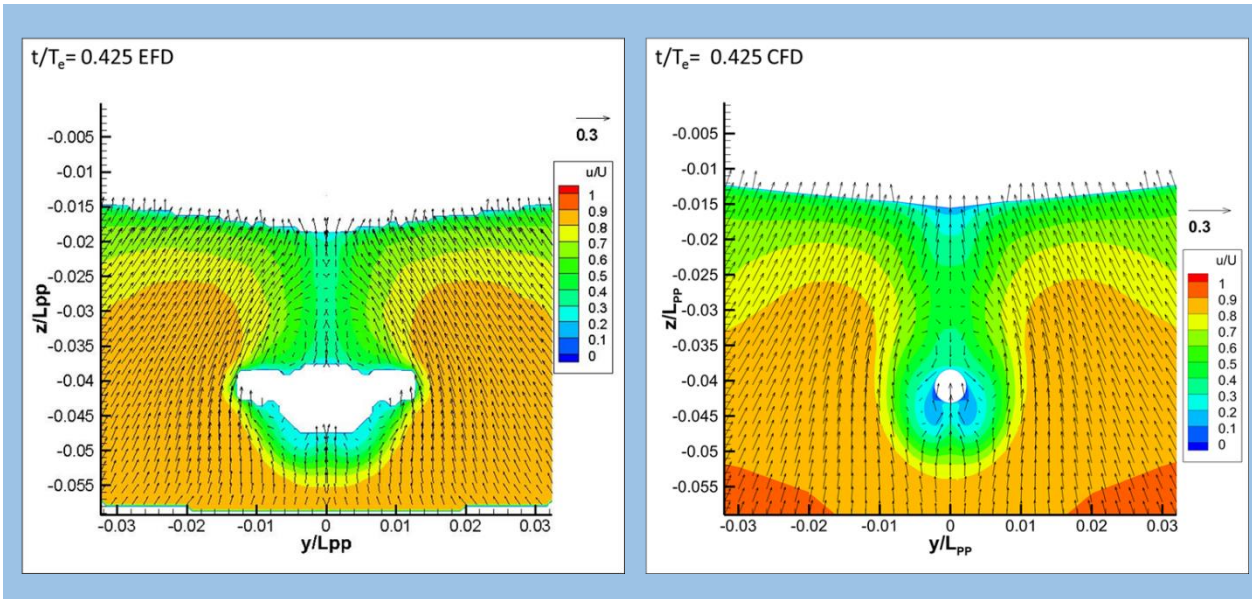

Figure 22 Comparison of EFD and CFD nominal wake at λ/L =1.15 (180 degree)

Comparison of EFD and CFD nominal wake at λ/L =1.15 (270 degree) is shown in Figure 23. At this moment (t/ Te~0.17), the ship stern is going upward. The low speed are (in blue shedding) is clearly noticeable below the dummy boss. The comparison shows that the velocity distribution at the propeller plane, along with the boundary layer distribution predicted by CFD is very similar to that measured in EFD. The bilge vortex moves up and down relative to the stern vertical motions. The moving region is near the side and upper area of the dummy boss around 0.5 propeller radius position, i.e. u/U=0.3~0.6 with green flooded contour. The secondary vortex is induced by the vertical motions and bilge vortex. It is shedding above and below the boss in the low speed area (u/U<0.3, blue flooded contour).

One thing is noticeable about the bilge vortex. The bilge vortex rotates clockwise in the portside labelled with positive vorticity ($+\omega_x$), and the secondary vortex would be opposite ($-\omega_x$: counterclockwise). The bilge vortex behavior of KCS is totally different compared to KVLCC2 in

previous study. In one period, the bilge vortex can be observed at the side or above the propeller dummy boss. It can never be observed below it, unlike the previous study about KVLCC2, the bilge vortex would move up and down relative to ship stern movement, even move out of the propeller radius [Wu, Sadat-Hosseini, Stern, and Toda, 2017]. This is due to the fine shape of KCS at the stern. The wide transom stern of KCS is almost like a T shape and thus very low mass at the stern. Because of such slimmer hull form, the vorticity magnitude of the bilge vortex on KCS (ω_x~+40) is much smaller than KVLCC2 (ω_x>+80). It is even smaller than its own secondary vortex $|\omega_x|$ (~|-80|), which has similar magnitude $|\omega_x|$ with both bilge and secondary vortex of KVLCC2. Thus, KCS and KVLCC2 have similar ω_x magnitude for secondary vortex. The bilge vortex can be observed either at the side or above the propeller dummy boss in KCS.

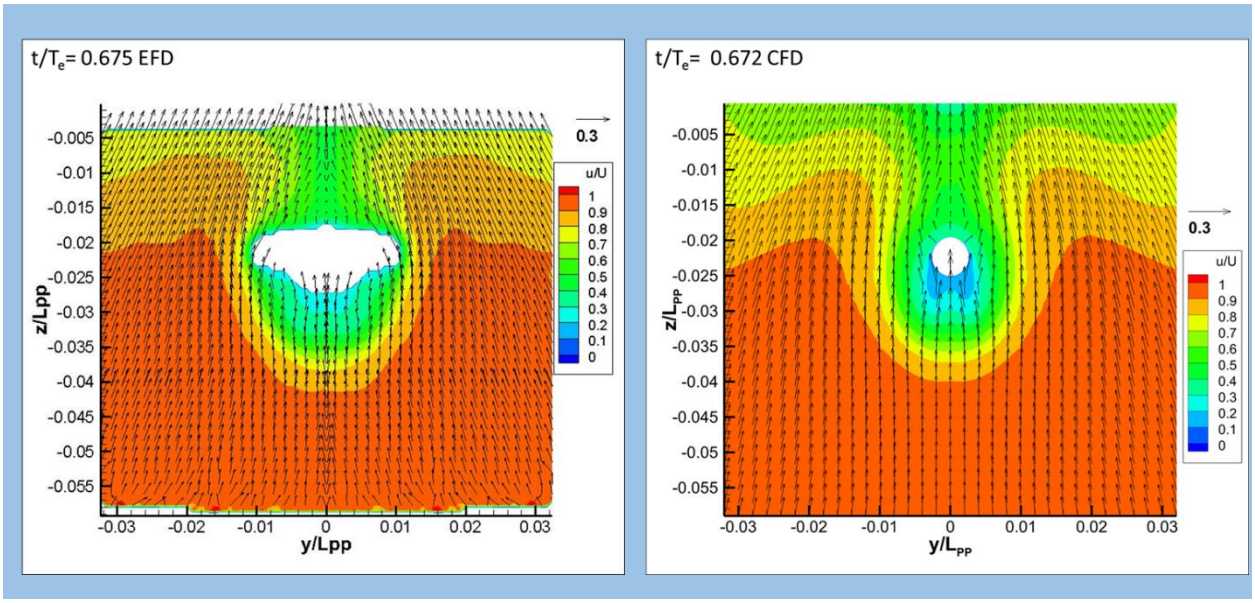

Figure 23 Comparison of EFD and CFD nominal wake at λ/L =1.15 (270 degree)

Similar validation study has been done for all the wave conditions. In this paper, one short wave condition (λ/L =0.65) and one long wave condition (λ/L =1.37) will be discussed.

Comparisons of EFD and CFD nominal wake at λ/L =0.65 for one encounter period are shown in Figure 24-Figure 27.

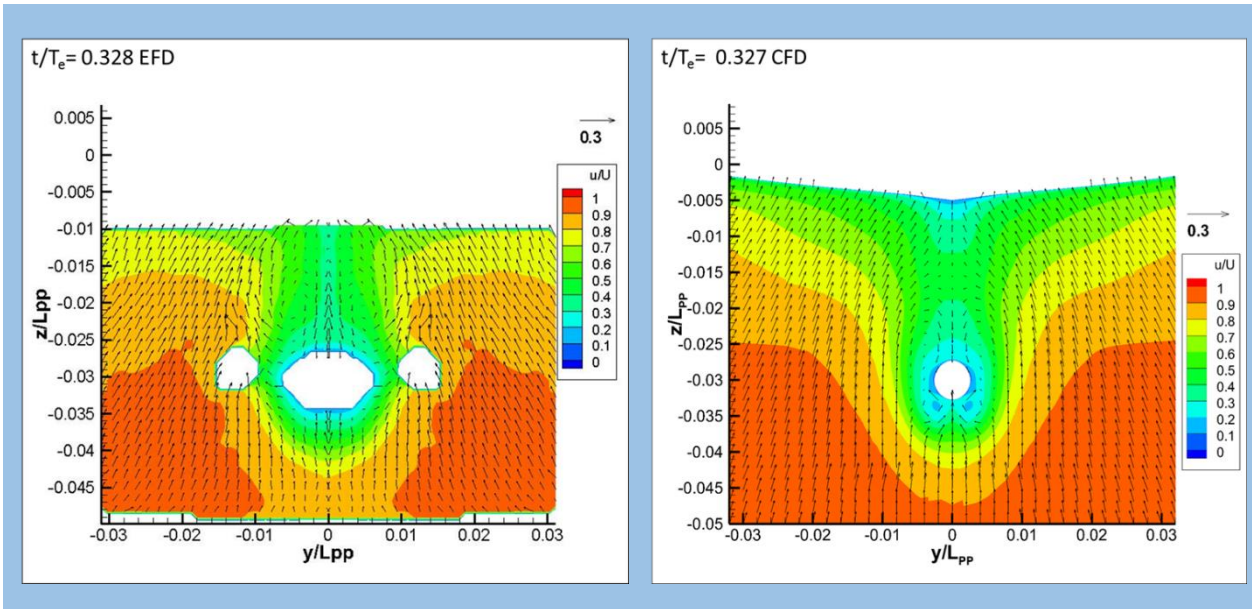

Figure 24 Comparison of EFD and CFD nominal wake at λ/L =0.65 (0 degree)

As discussed in 5.1 Ship Motions, the motion responses at λ/L =0.65 is very small. Therefore, the nominal wake at the propeller plane in this case is almost similar to that in calm water case. The ship stern slightly oscillates vertically and thus the boundary layer and the velocity distribution at the propeller plane is almost similar for all time steps, while the ship is slowly going upward. The bilge vortex can be observed above the propeller dummy boss.

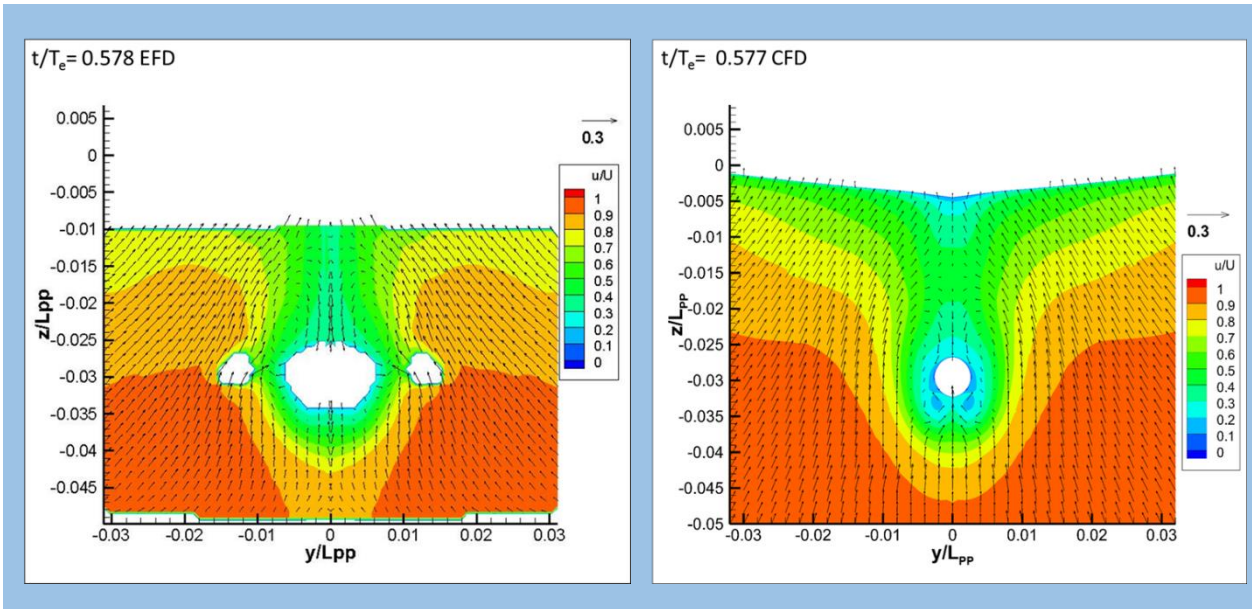

Figure 25 Comparison of EFD and CFD nominal wake at λ/L =0.65 (90 degree)

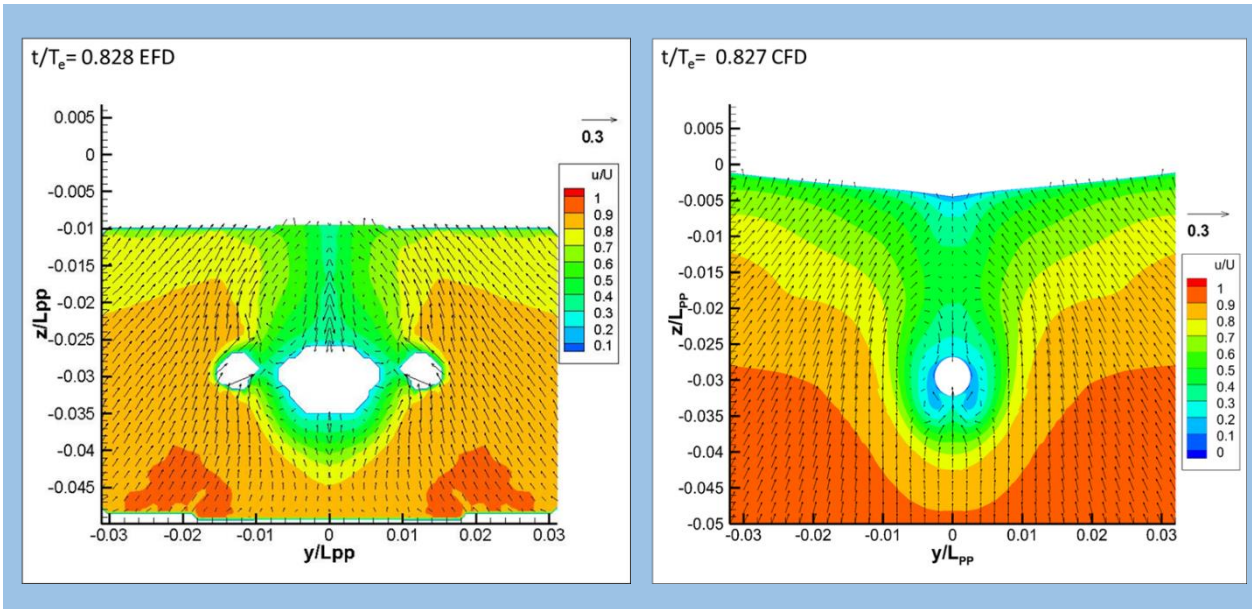

Figure 26 Comparison of EFD and CFD nominal wake at λ/L =0.65 (180 degree)

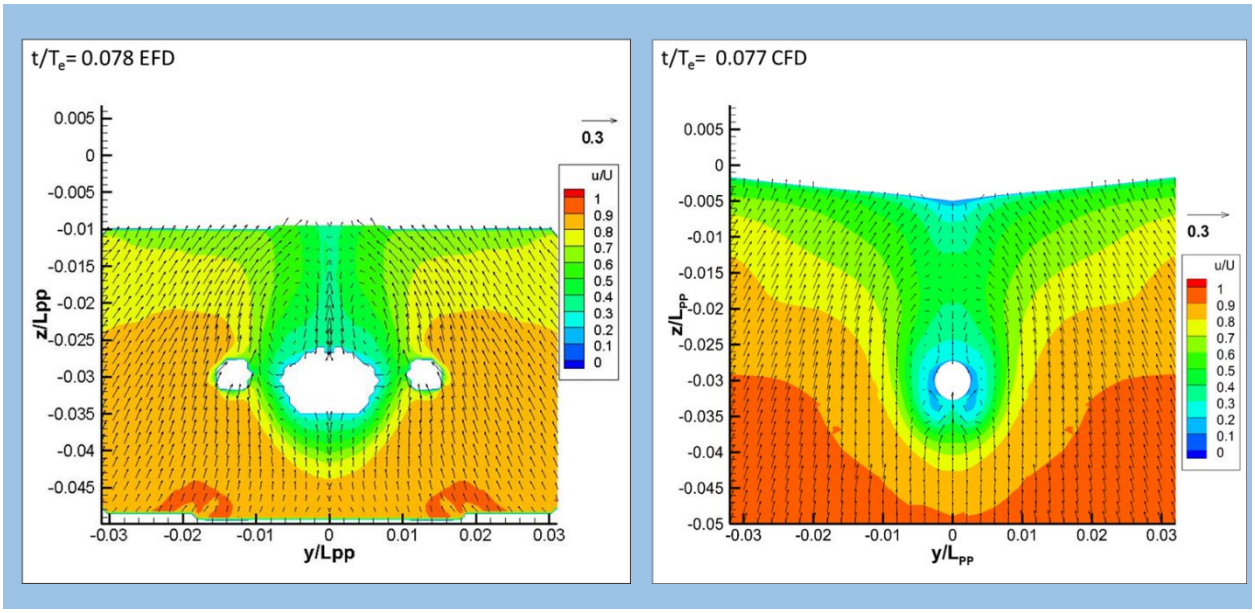

Figure 27 Comparison of EFD and CFD nominal wake at λ/L =0.65 (270 degree)

For the long wave condition, comparisons of EFD and CFD nominal wake at λ/L =1.37 for one encounter period are shown in Figure 28Figure 31. When t/ Te~0.06, the ship stern goes downward which can be easily understood by the low speed area (in blue color shedding) above the dummy boss. The bilge vortex can be observed on the sides of the propeller dummy boss while the secondary vortex is suppressed under the boss.

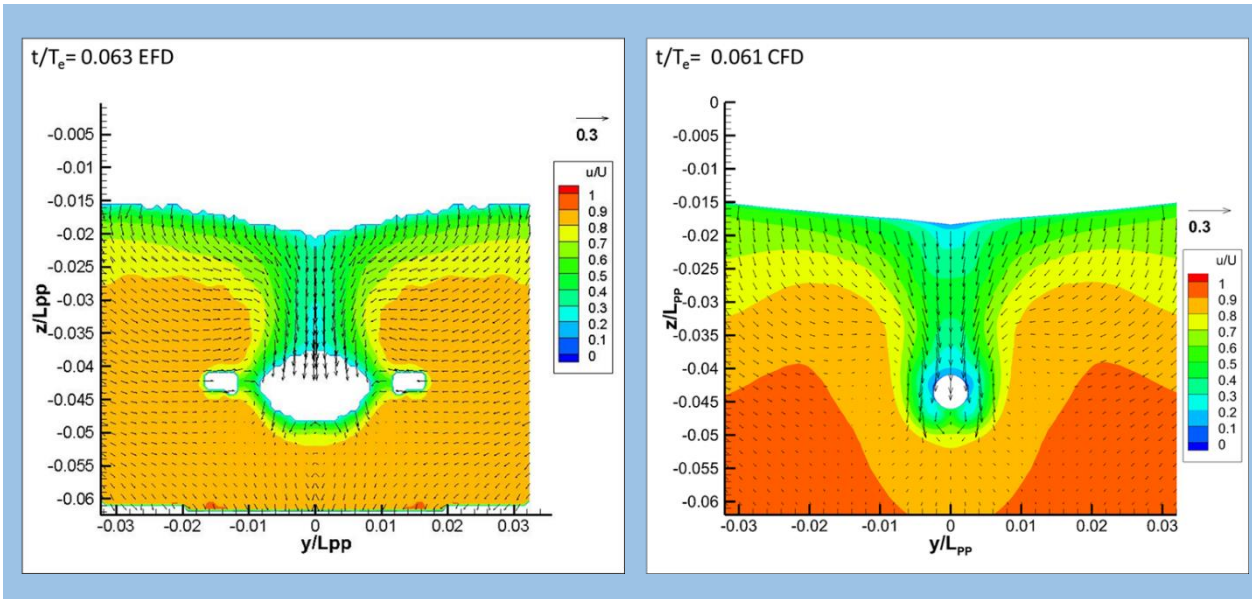

Figure 28 Comparison of EFD and CFD nominal wake at λ/L =1.37 (0 degree)

When t/ Te~0.31, the ship stern is going upward. The low speed are (in blue shedding) is visibly noticeable below the dummy boss. The bilge vortex can be observed above the propeller dummy boss very clearly.

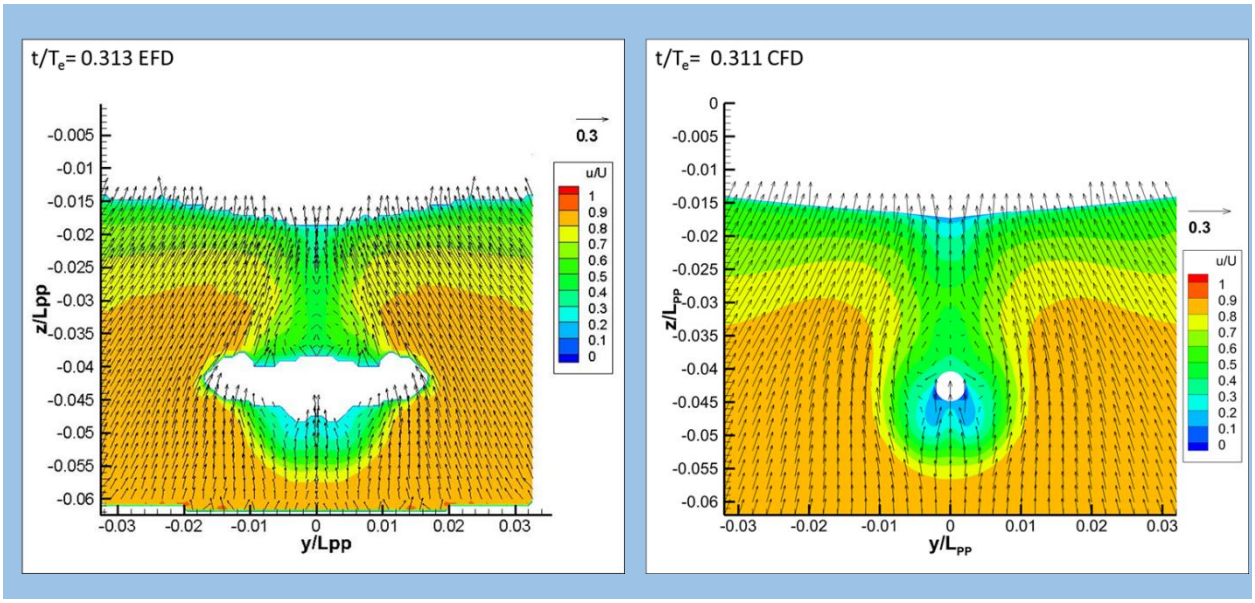

Figure 29 Comparison of EFD and CFD nominal wake at λ/L =1.37 (90 degree)

At t/ Te~0.56, the ship stern is still going upward and almost reaches to the highest vertical position.

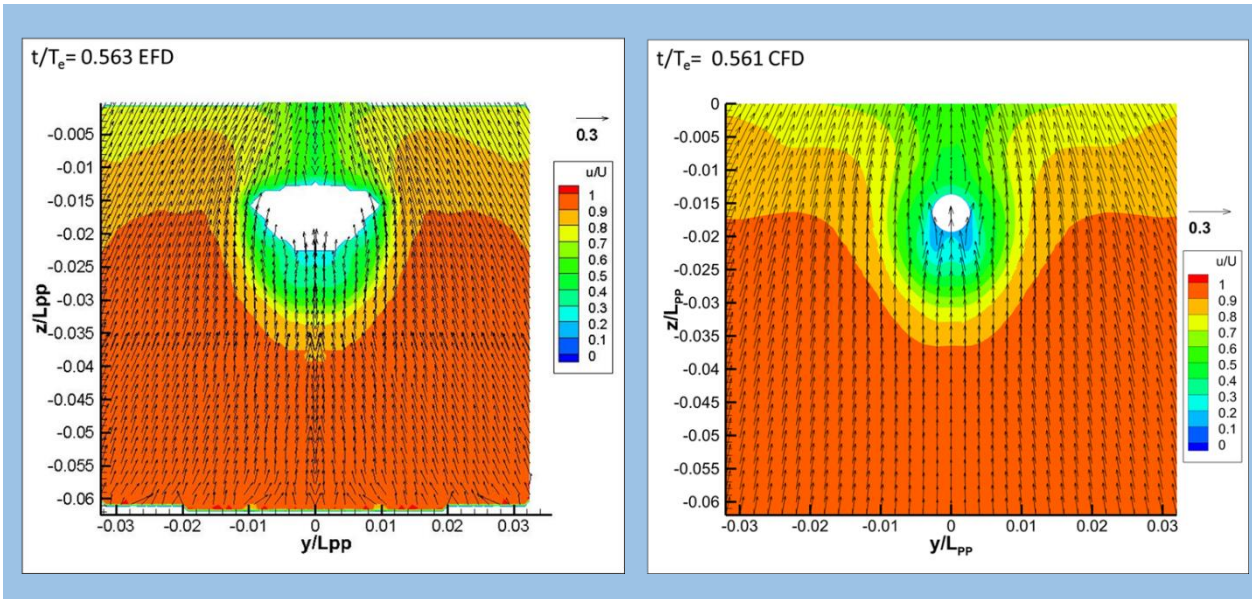

Figure 30 Comparison of EFD and CFD nominal wake at λ/L =1.37 (180 degree)

When t/Te = 0.81, the ship stern again starts to move downward and the low speed area (in light blue shedding) can be observed above the propeller dummy boss. Meanwhile, the bilge vortex has been shifted to the side of the propeller dummy boss. At this moment, CFD slightly over predicts the velocity distribution in the outer part of flow field (dark red region).

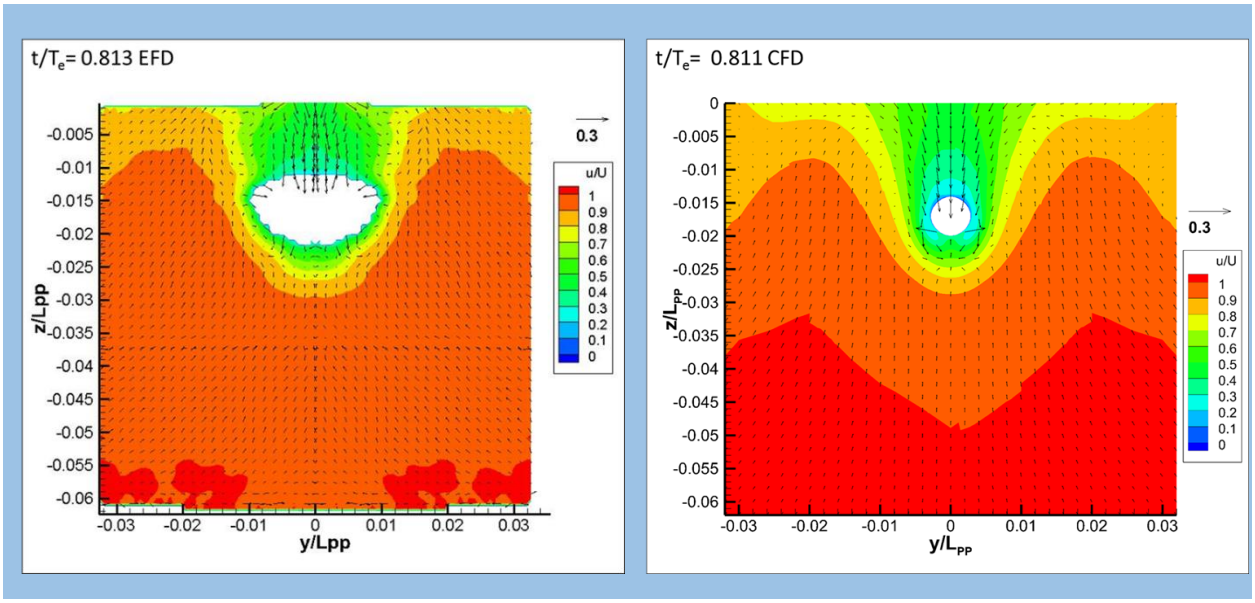

Figure 31 Comparison of EFD and CFD nominal wake at λ/L =1.37 (270 degree)

Time history of nominal wake factor in waves has also been calculated. By integrating the axial velocity (u_N) distribution inside the propeller radius, nominal wake factor ($1 - w_N$) can be calculated using the following formula-

$$1 - w_N = \frac{1}{\pi(r_p^2 - r_0^2)} \int_{r_0}^{r_p} u_N \, dA \tag{41}$$

Here,

r_p = Radius of propeller

r_0 = Radius of propeller hub

Using the above-mentioned formula, the nominal wake factor ($1\text{-}w_N$) has been calculated for one encounter period and compared with the effective wake factor measured in EFD. The dotted horizontal line in this figure represents the mean of the EFD effective wake factor. From this figure, it is observed that good agreement in phase has been obtained. The oscillation of the wake factors for λ/L =1.15 was close to sinusoidal but with some higher harmonic component: different steepness for increasing and decreasing slope (Figure 32). In [Sadat-Hosseini et al., 2015], the oscillation of CFD nominal wake factor was almost sinusoidal for λ/L =1.37.

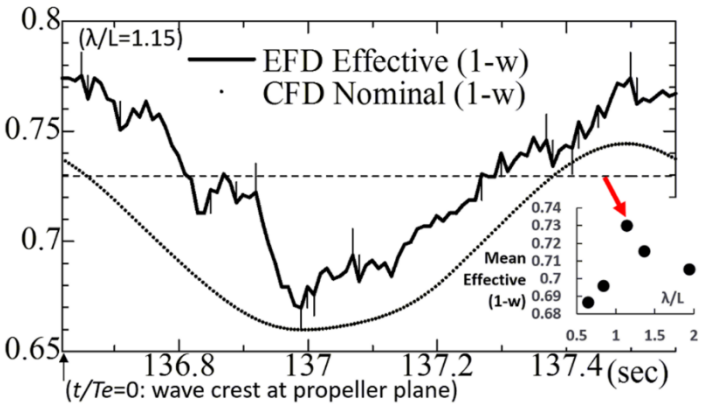

Figure 32: Comparison of the time history of CFD nominal wake and EFD effective wake in waves at λ/L =1.15

5.4 Self-Propulsion

For the self-propulsion, computation has been done for all five λ/L ratios and in calm water. However, for the experiment, only λ/L = 0.65, 1.15, 1.37 and calm water were chosen. propeller has minor influence on vertical motions z/*A*, θ/*Ak*. Time history comparison of CFD and EFD wave motion, Heave, Pitch, K_T, K_Q for λ/L = 0.65, 1.15, 1.37 are shown in Figure 33, Figure 34 and Figure 35 respectively.

Figure 36 and Figure 37 show the mean value of thrust (N) and torque (N-m) for different wave lengths. CFD and EFD have very good agreement. To achieve self-propulsion in waves, the thrust and torque, i.e. propeller loads, need to be increased to conquer the resistance increase. Thus, all thrust and torque from short to long waves is larger than calm water case. The trend is coincident with the added resistance coefficient (Figure 17).

For the self-propulsion condition, the velocity field was measured on three sections as shown in Figure 38: x/*L* =0.972 before the propeller plane (x/*L* =0.9825), x/*L* =0.990 right after the propeller plane (x/*L* =0.9825) and x/*L* =1.025 after the rudder.

Figure 39 presents the flow field comparison in calm water after the rudder (x/*L* =1.025) between S- SPIV and CFD side by side. They are plotted by the flooded contour for axial velocity (u/U) and vector field for cross flow (v/U, w/U). Both results show the similar flow pattern. The high axial velocity mainly is in the starboard because of clockwise rotating propeller inside stern upward flow. Corresponding to the conclusion for higher CFD (1-w), CFD predicted a higher u/U area with a curvy band shape. The clockwise rotating flow is interfered by the rudder in the middle, so the cross flow was twisted to form upward flow portside and downward starboard. The hub vortex is separated becoming two cores as well: the portside hub vortex is in the lower position and starboard hub vortex is located higher. A vortex was induced by outer upward flow and starboard downward cross flow around (y/*L* , z/*L*) = (0.01, -0.02). It is the corner of high u/U contour.

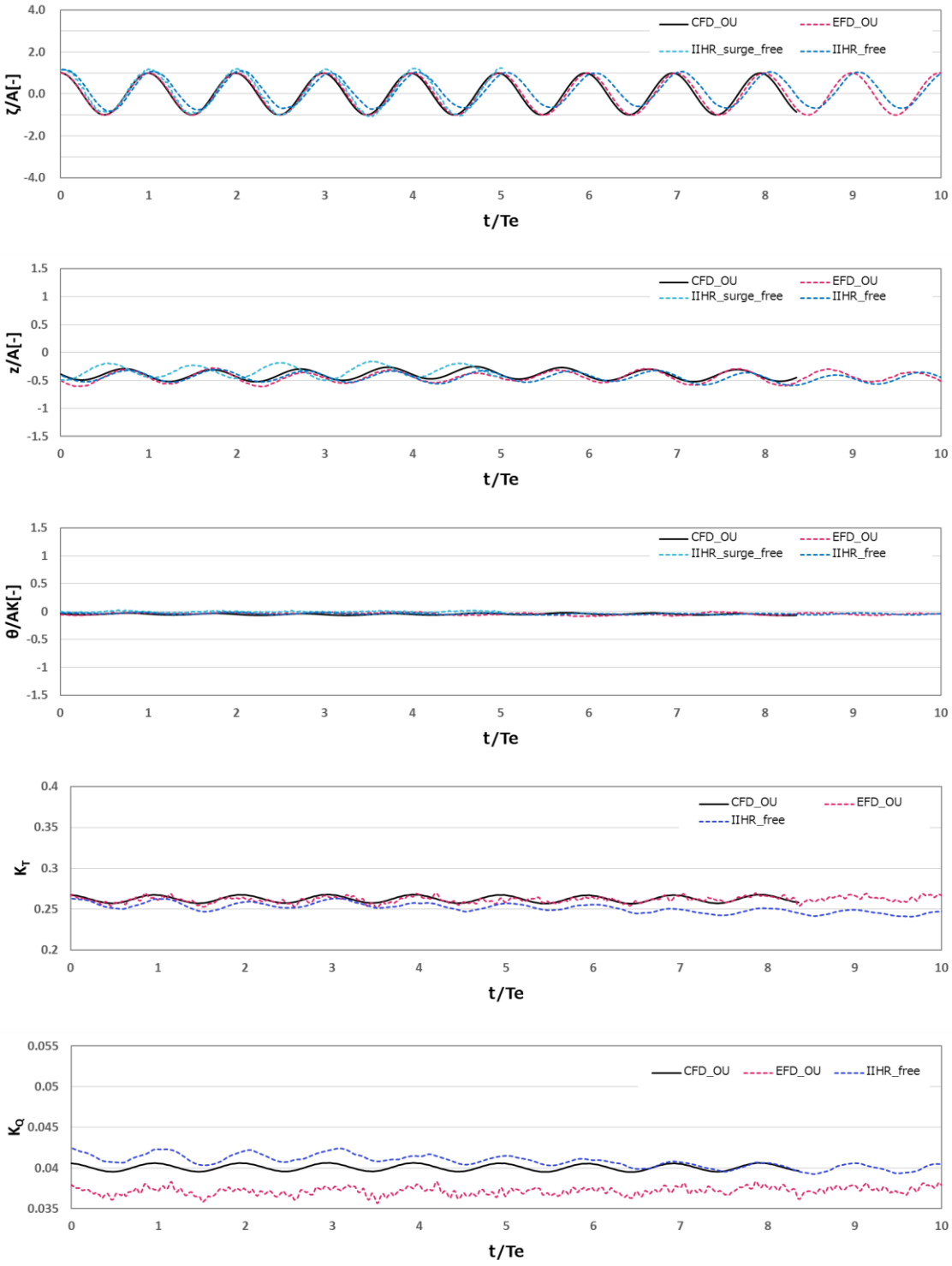

Figure 33: Time history comparison of CFD and EFD wave motion, Heave, Pitch, KT, KQ for $\lambda/L = 0.65$

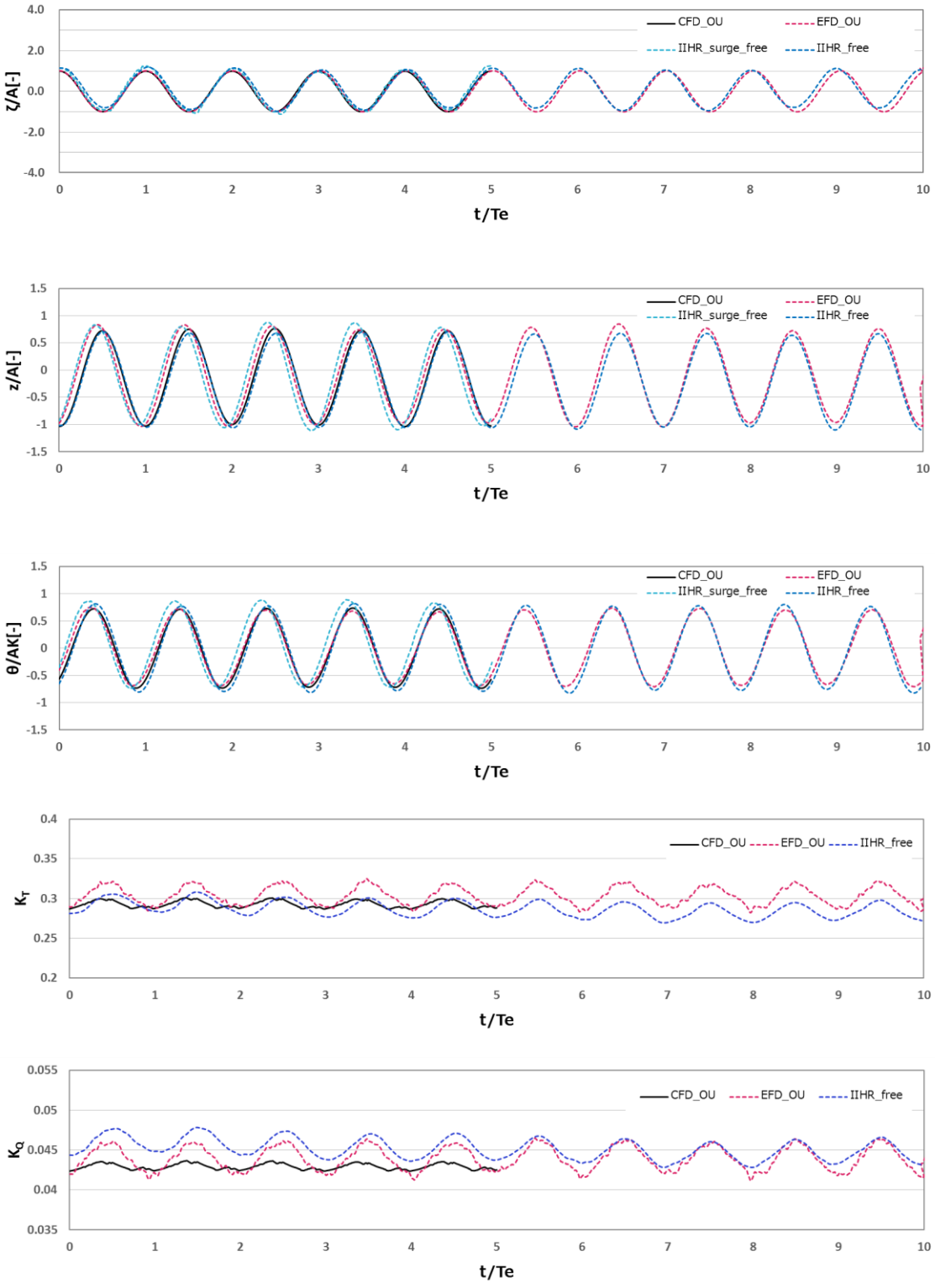

Figure 34: Time history comparison of CFD and EFD wave motion, Heave, Pitch, KT, KQ for λ/L = 1.15

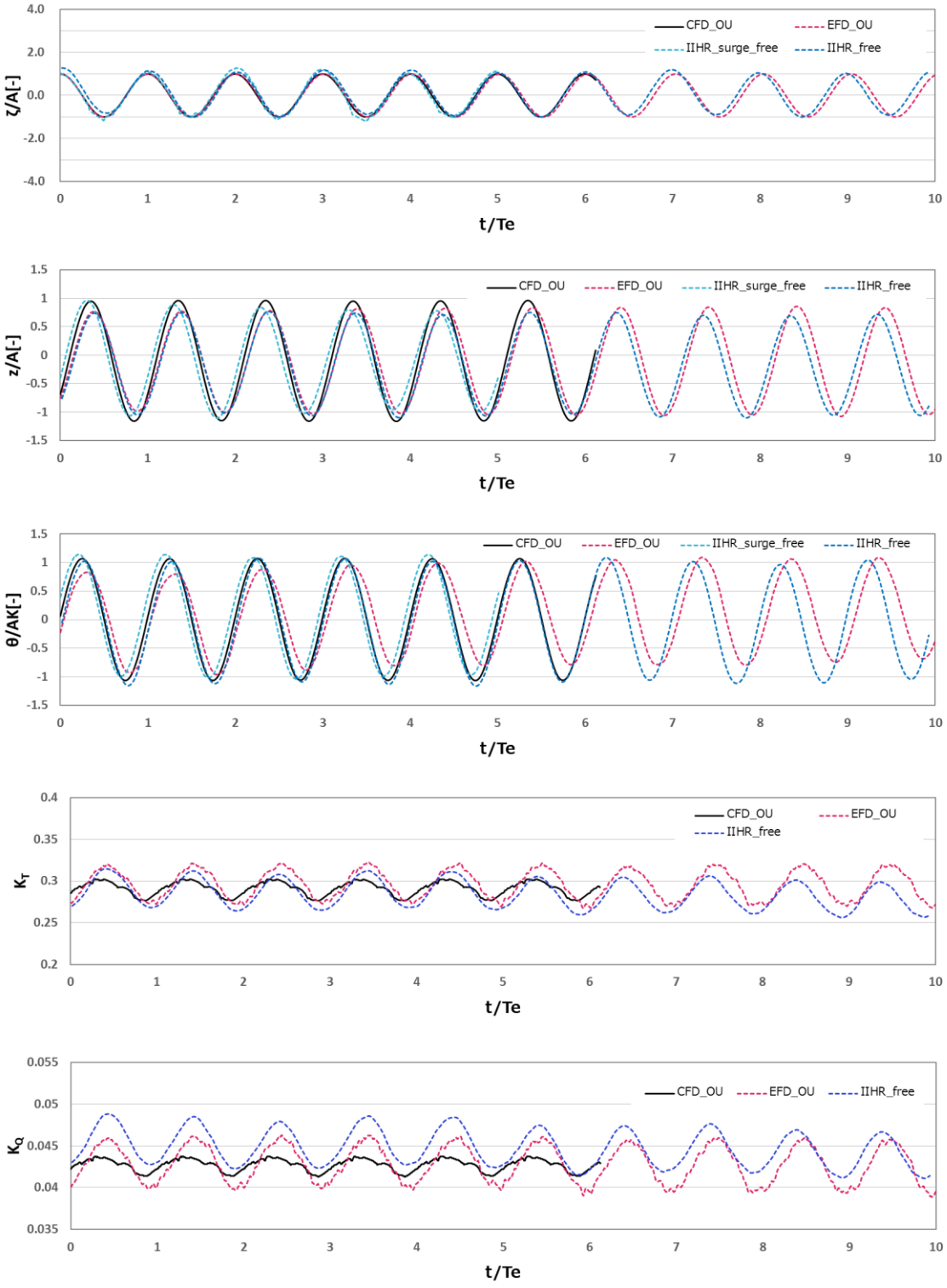

Figure 35: Time history comparison of CFD and EFD wave motion, Heave, Pitch, KT, KQ for λ/L = 1.37

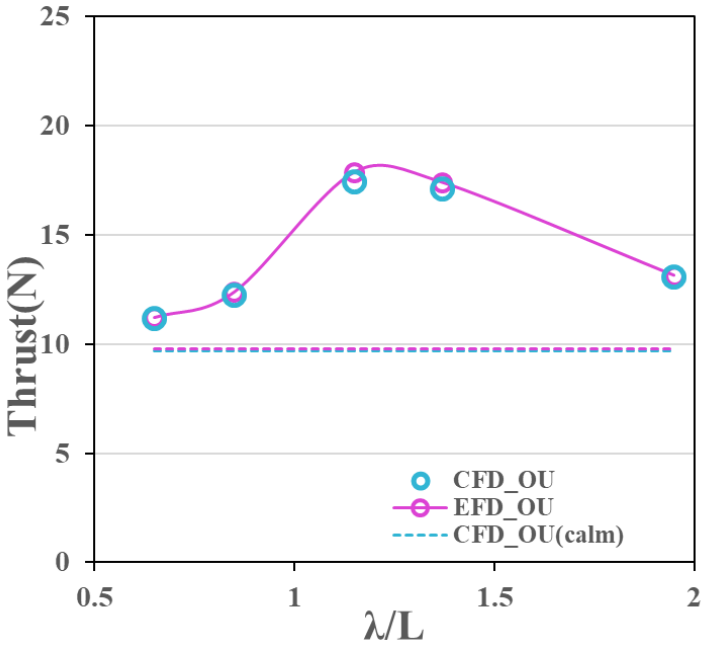

Figure 36: Thrust for different wave lengths

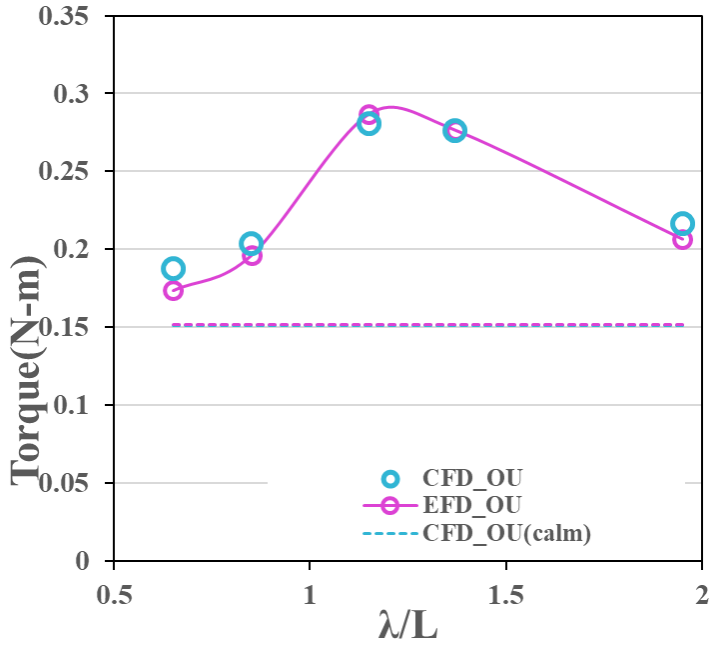

Figure 37: Torque for different wave lengths

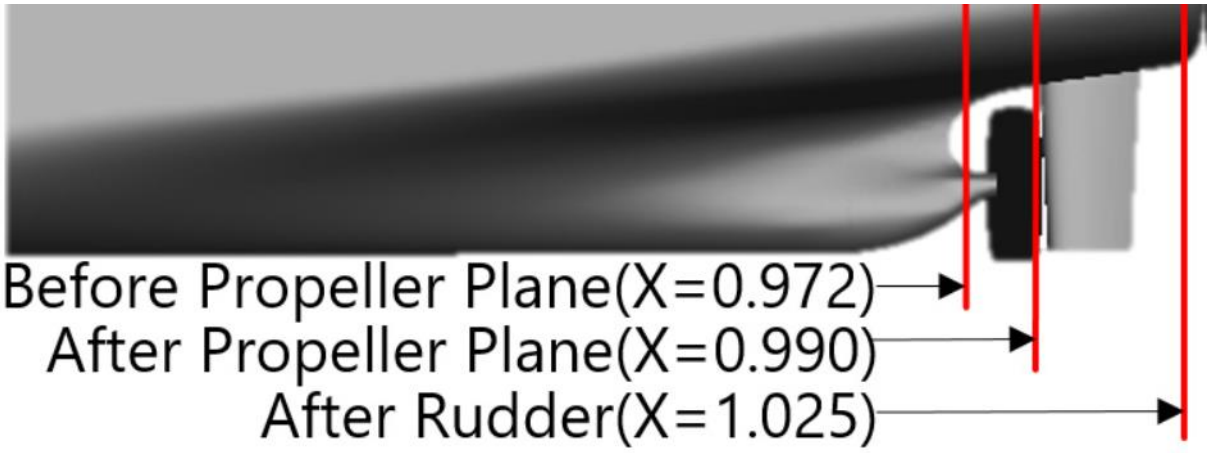

Figure 38: Three S-PIV measurement sections

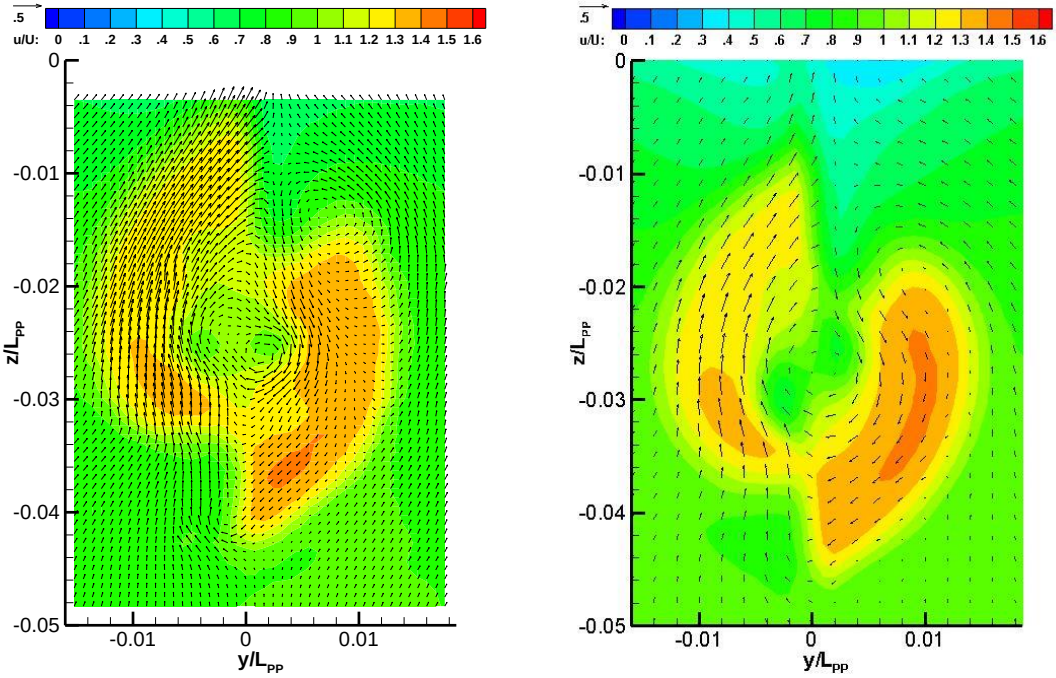

Figure 39: Velocity field after rudder in calm water (left: S-PIV, right: CFD)

In waves, the flow pattern was kept but u/U increases for the whole distribution. In the following figures, S-PIV and CFD flow field comparison was plotted for 4 time instants t/Te in one encounter period for each wave length. Figure 27, 28, and 29 show the comparison after the rudder (x/*L* =1.025) for λ/L =0.65, 1.15 and 1.37, respectively.

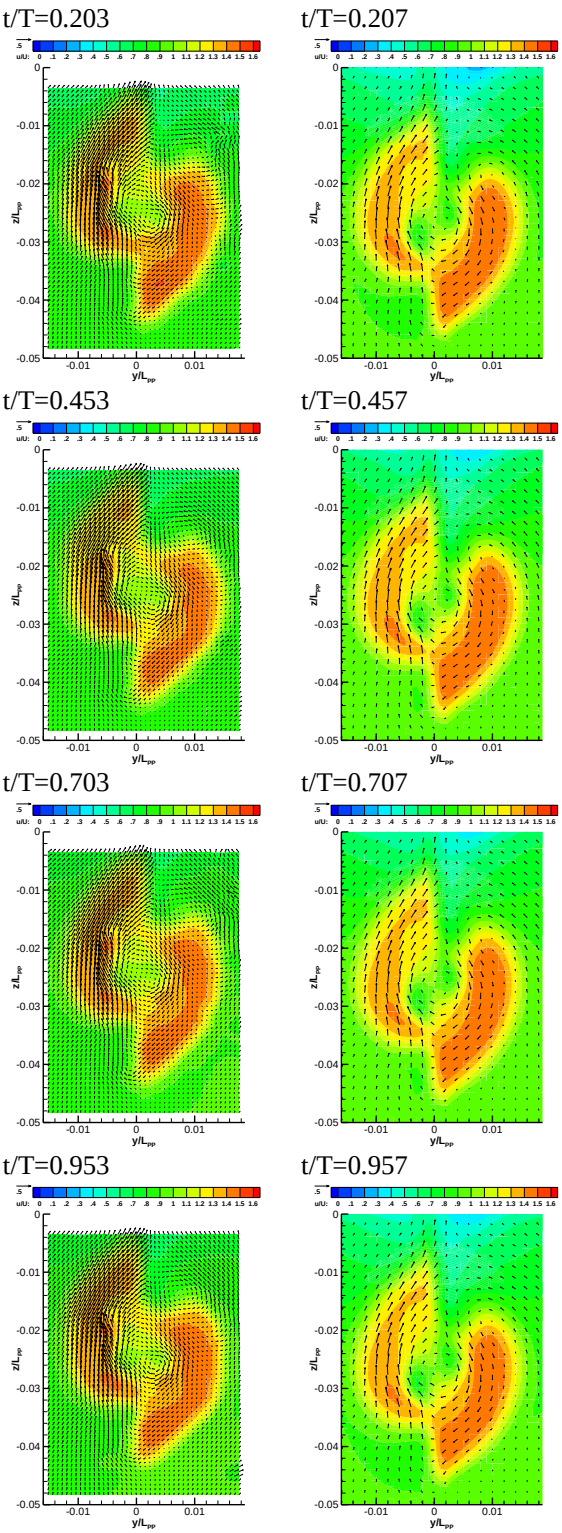

Figure 40: Velocity field after the rudder for λ/L =0.65 (left: S-PIV, right: CFD)

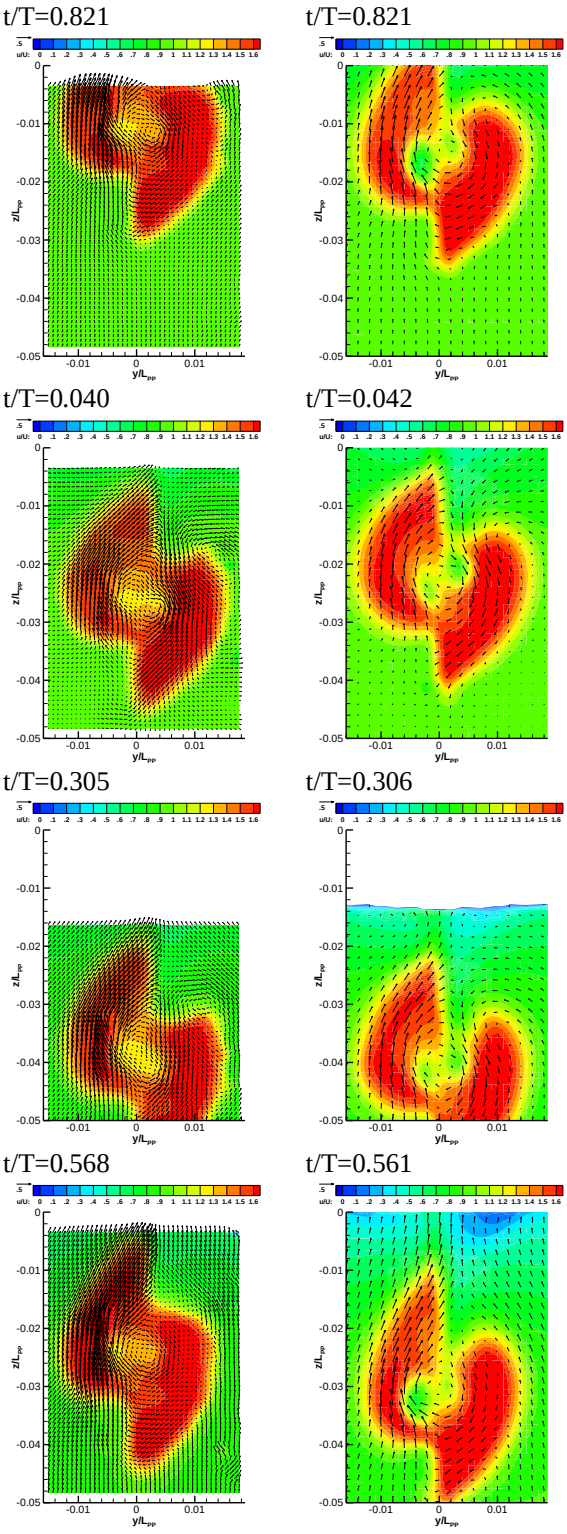

Figure 41: Velocity field after the rudder for λ/L =1.15 (left: S-PIV, right: CFD)

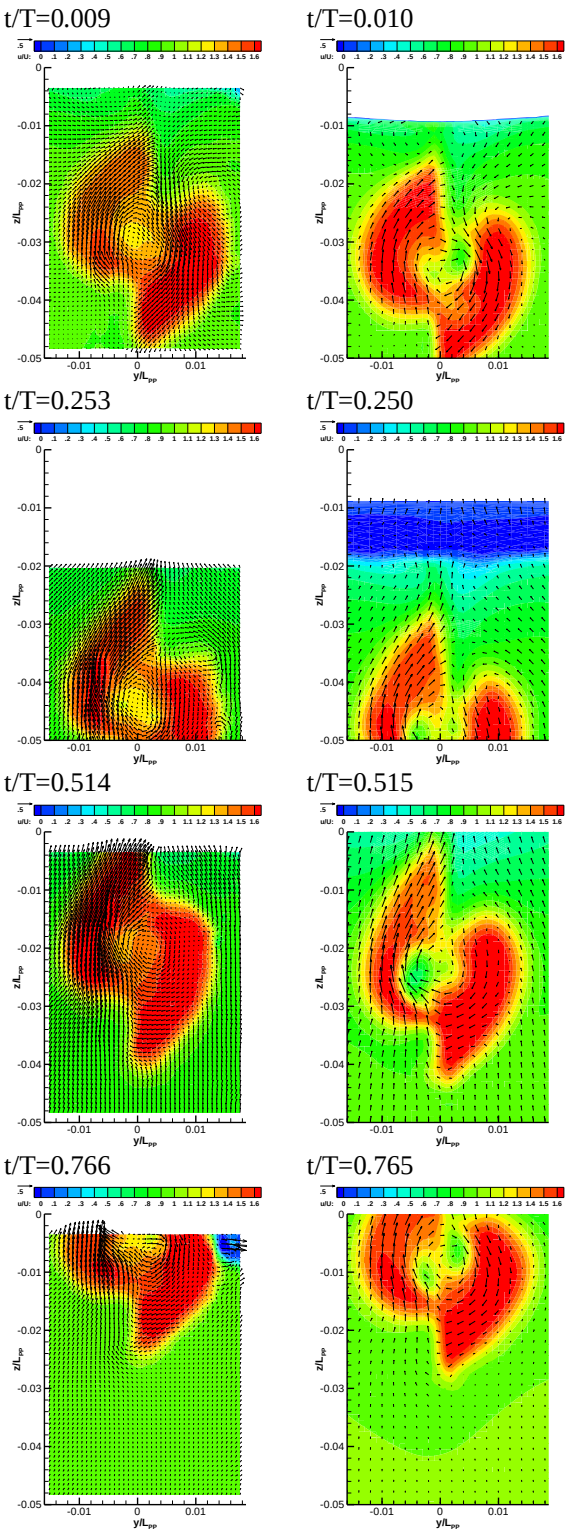

Figure 42: Velocity field after the rudder for λ/L =1.37 (left: S-PIV, right: CFD)

In short waves λ/L =0.65, because of small ship vertical motions the flow pattern is similar to calm water case with slightly higher velocity magnitudes for the different t/T_e. In long waves λ/L =1.15 and 1.37, the propeller wake moves up and down obviously, i.e. large vertical motions. The flow pattern was still maintained but the velocities increase much higher overall. It is consistent with the conclusion for the higher (1-w) in long waves. Compared to CFD results, the u/U inside the hub vortex core are higher in S-PIV results. Two sides of hub vortex are closer each other in z-direction in S-PIV result. For CFD, portside hub vortex is generally located higher than starboard side.

The right-rotating propeller influences the upstream flow field asymmetrically. Figure 43 and Figure 44 are the comparison before the propeller plane (x/L =0.972) for λ/L =1.15 and 1.37. For S-PIV, only portside flow field was measured. The right-rotating propeller flow interacts with the relative velocity between the stern vertical motions and stern upward flow, thus the upstream velocity is accelerated asymmetrically. During the stern motions down to or up from the low position, u/U is clearly higher in starboard side. The stern upward flow majorly causes the starboard inflow with higher angle of attack into the propeller. For example, λ/L =1.15 at t/T=0.41, 0.63 and λ/L =1.37 at t/T=0.327. During the stern motions down, stern downward velocity becomes more dominant and induces portside u/U slightly higher. For instance, λ/L =1.15 at t/T=0.18 and λ/L =1.37 at t/T~0.07 and 0.82. For some scenario, the flow field is nearly symmetric. When ship stern starts moving down from high position, like λ/L =1.15 at t/T=0.9, or moving to near the top, like λ/L =1.37 at t/T=0.57, the propeller is far away from stern upward flow with small stern vertical velocity. In addition of the asymmetric velocity distribution, the bilge vortices are also influenced by the right-rotating propeller. The vector field of λ/L =1.15 at t/T=0.41, 0.63 and λ/L =1.37 at t/T=0.327 in Figure 43 and Figure 44 (x/L =0.972) shows the bilge vortices of the both sides are asymmetric in rotating direction and pattern. Also, the vectors along y/L_{PP}=0 are twisted toward starboard. Although Figures 13, 14, 15 and 16 are at x/L =0.9825, they are the references showing without propeller those vectors are straight up and down, symmetric along y/L_{PP}=0.

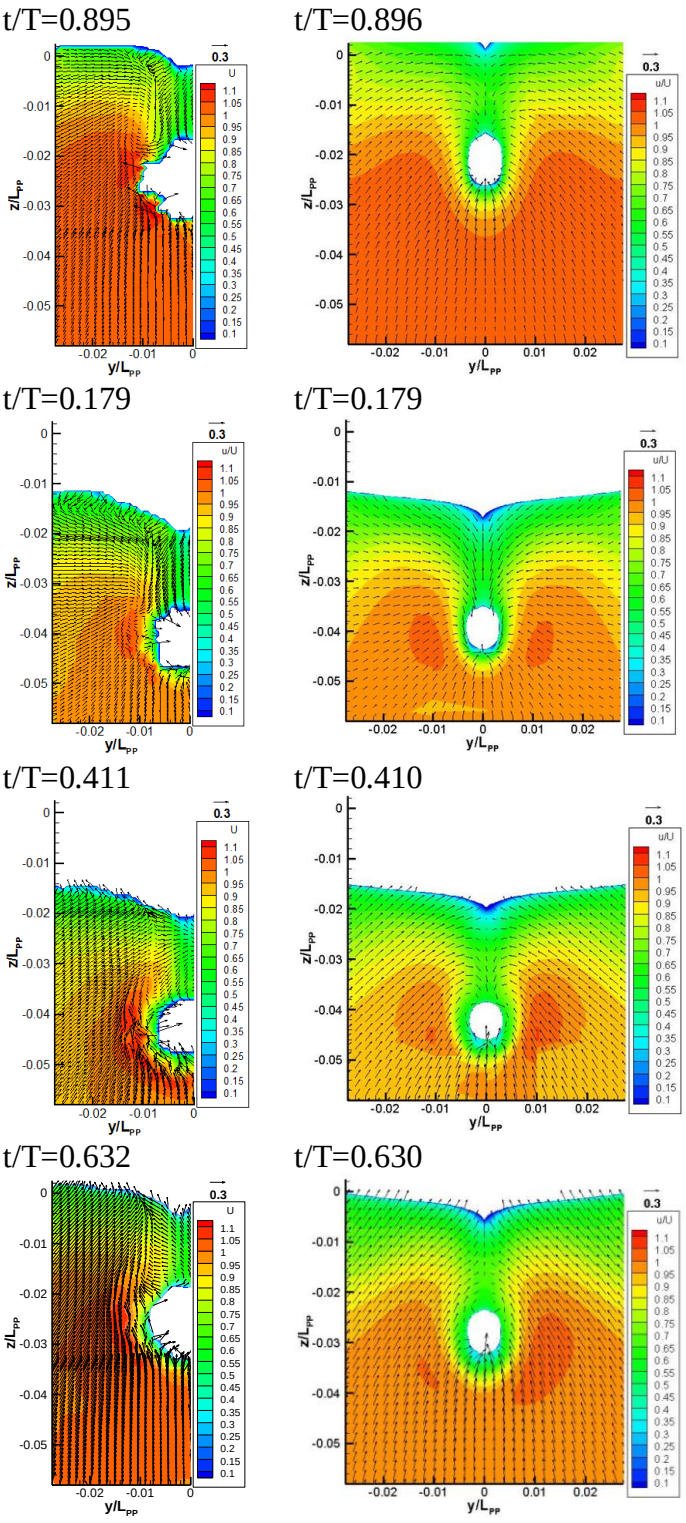

Figure 43: Velocity field before propeller plane (x/L =0.972) for λ/L =1.15 (left: S-PIV, right: CFD)

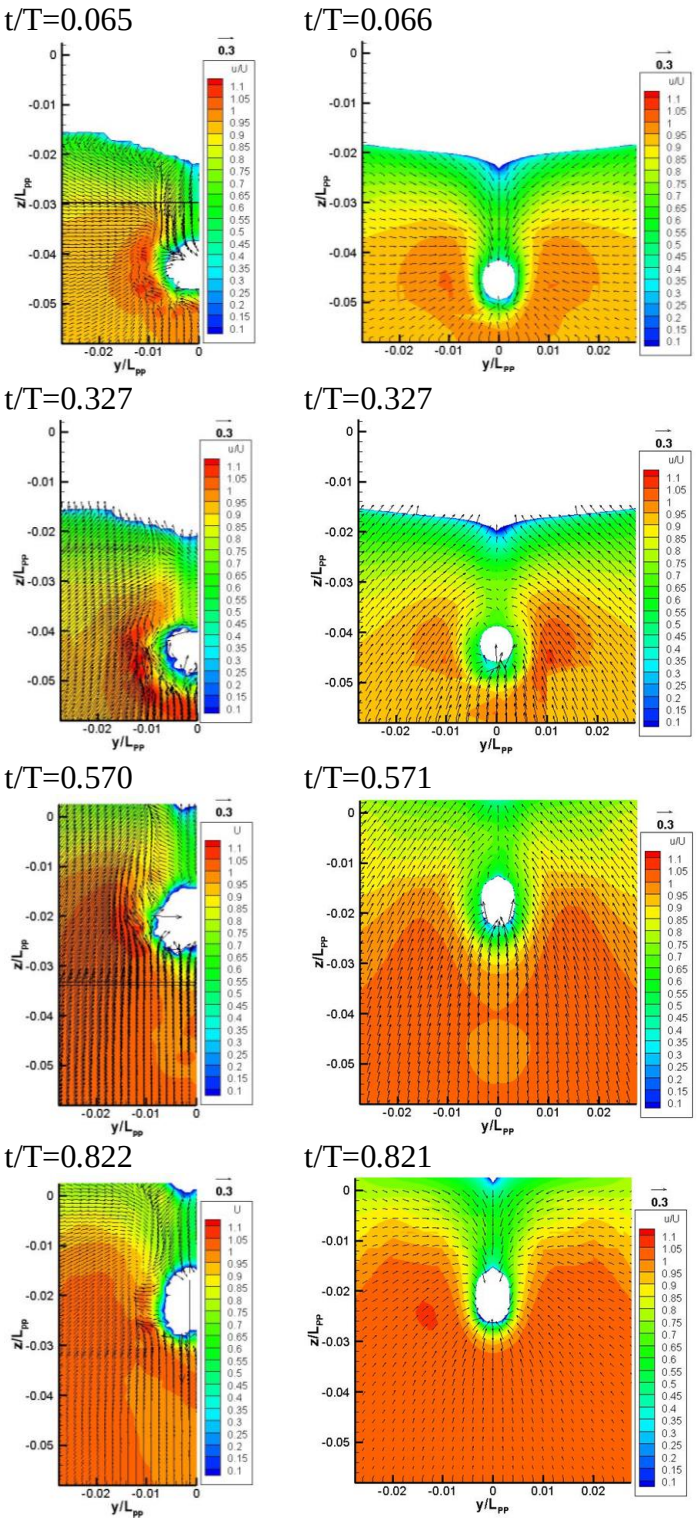

Figure 44: Velocity field before propeller plane (x/L =0.972) for λ/L =1.37 (left: S-PIV, right: CFD)

Figure 45 and Figure 46 are the comparison after propeller plane (x/L =0.99) for λ/L =1.15 and 1.37. x/L =0.99 is between propeller and rudder leading edge. Because of the stern vertical motion, the rudder and propeller boss would interfere the flow field occasionally. For CFD, the coarse grids from outside blocks would come into the propeller disk during the stern vertical motions. The future improvement of overset grid topology is required. Without rudder influence (e.g. λ/L =1.15 at t/T~0.9, λ/L =1.37 at t/T=0.57 and 0.82), the high u/U mainly is in the upper starboard side. In the other t/T when the rudder inserts into the propeller wake, the right-rotating flow would form higher angle of attack in upper starboard and lower port-side. Thus, the high u/U is observed. Also, the hub vortex is separated into two cores.

The effective wake factor (1-w) of CFD and EFD was calculated by thrust identity method for three wave lengths and calm water. The K_T-J curve was obtained by the open water propeller test in Osaka University Towing Tank:

$$K_T = -0.01017J^2 - 0.4168J + 0.5116 \tag{42}$$

Figure 47, Figure 48 and Figure 49 present the CFD and EFD wake factor for λ/L =0.65, 1.15 and 1.37, respectively. Their mean values are plotted in **Error! Reference source not found.**. For calm water, it can be seen: CFD (1-w) > EFD (1-w) > CFD (1-w_N). The propeller suction induces higher inflow velocity. In waves all CFD mean (1 - w) is larger than calm water value indicating faster propeller inflow in waves. Except for EFD (1-w) of λ/L =1.15 and 1.37, the entire oscillations are above the calm water value. The (1-w) oscillation amplitude increases as λ/L increases. Unlike KLVCC2 (Wu, et al., 2017), the bilge vortex movement in waves of KCS is less intense. Thus, in λ/L =1.15 (Figure 48) (1- w_N) oscillation is nearly simple harmonic which was also confirmed by Sadat-Hosseini, et al. (2015). For (1-w), only CFD (1-w) of λ/L =0.65, is almost sinusoidal because of small ship motions. EFD (1-w) all has signal noise. In long waves λ/L =1.15 and 1.37, CFD show some high frequency noise. However, neglecting the noise roughly, similar steepness for increasing and decreasing slope can be observed. The bilge vortex movement and stern vertical motions do not influence (1-w) much. EFD (1-w) amplitudes for λ/L =1.15 and 1.37 are larger than CFD. Their troughs are lower than calm water values with a phase lag earlier than CFD.

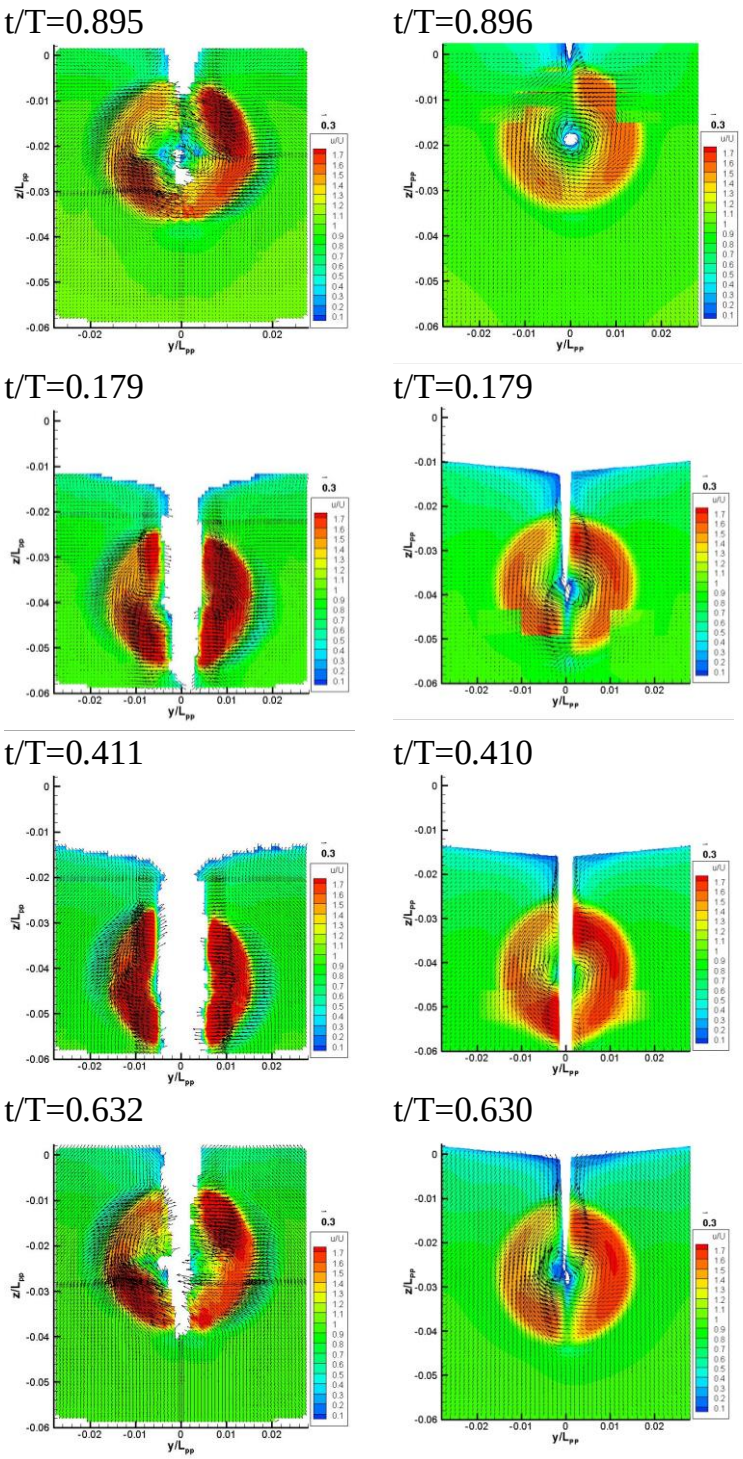

Figure 45: Velocity field after propeller plane (x/L =0.99) for λ/L =1.15 (left: S-PIV, right: CFD)

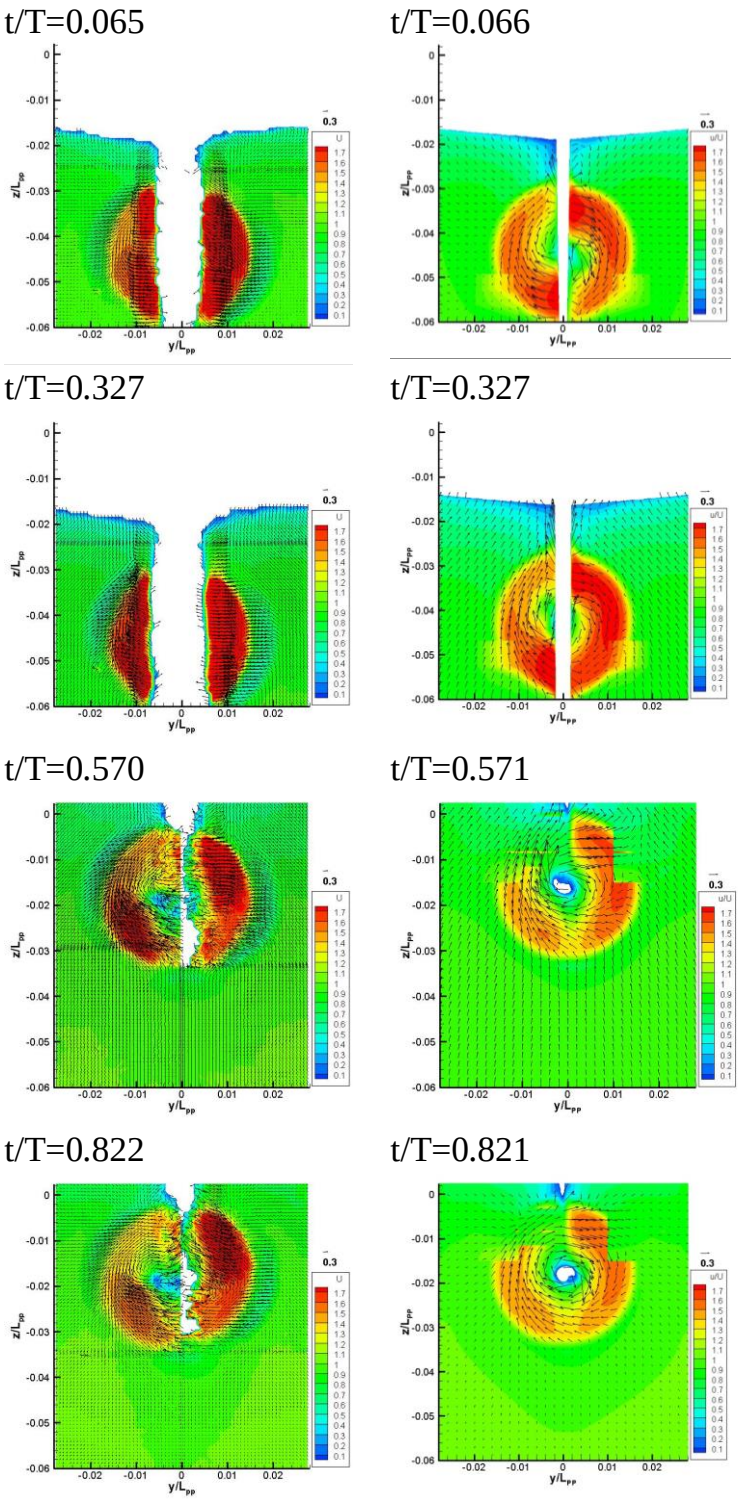

Figure 46: Velocity field after propeller plane (x/L =0.99) for λ/L =1.37 (left: S-PIV, right: CFD)

Further investigation is required to study if the bilge vortex effect is different in EFD and CFD using the propeller model. In Figure 50, mean (1-*w*) follows the same trend with the added resistance (Figure 17), i.e. the peak at λ/L =1.15. The CFD mean (1-*w*) is over-predicted around 2% against EFD (1-*w*) for λ/L =1.15 and 1.37.

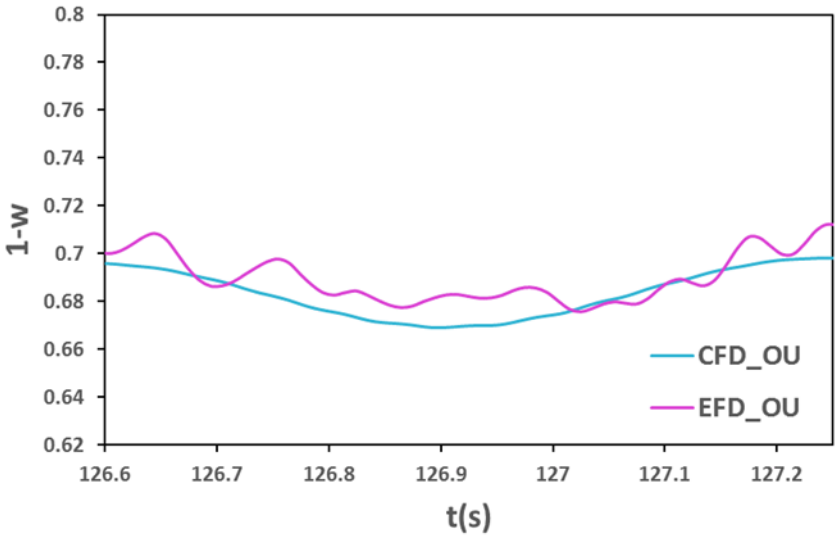

Figure 47: CFD and EFD effective wake factor for wave length λ/L =0.65

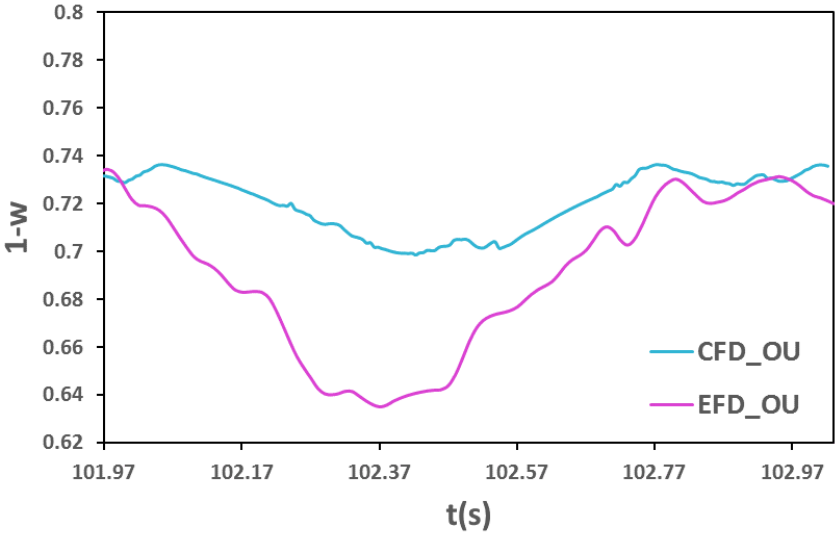

Figure 48: CFD and EFD effective wake factor for wave length λ/L =1.15

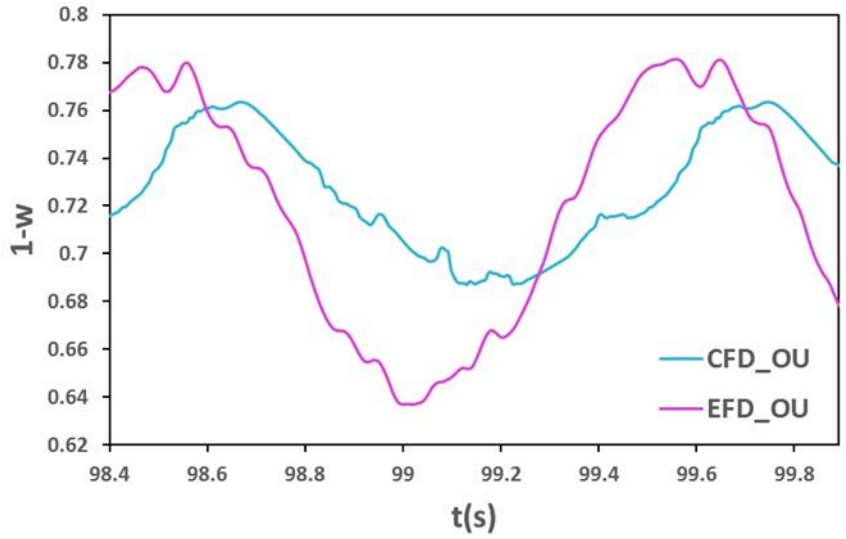

Figure 49: CFD and EFD effective wake factor for wave length λ/L =1.37

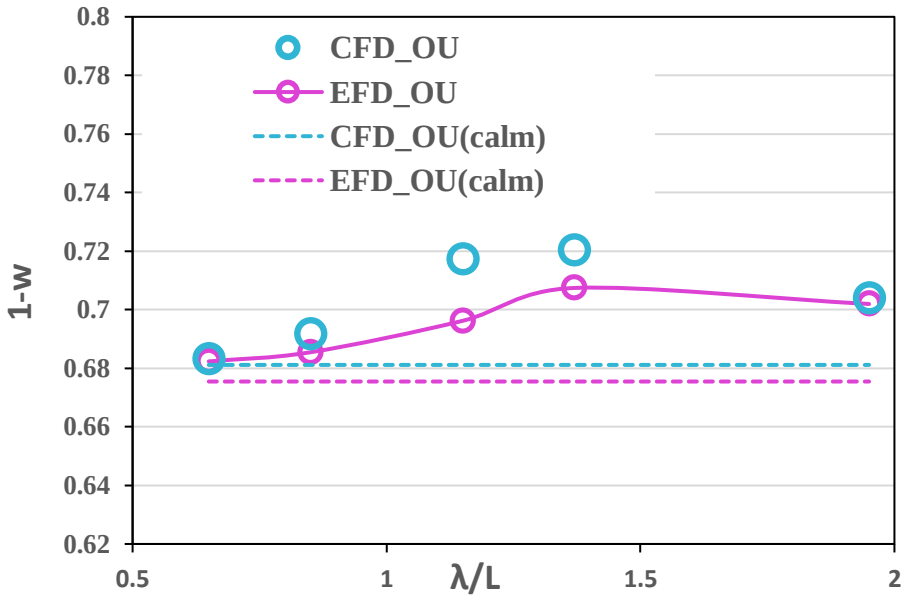

Figure 50: CFD and EFD mean effective wake factor for different wave lengths.

Added powering coefficients have been calculated for all λ/L ratios. Computational results show good agreement with the experimental results (Figure 51, Figure 52, Figure 53).

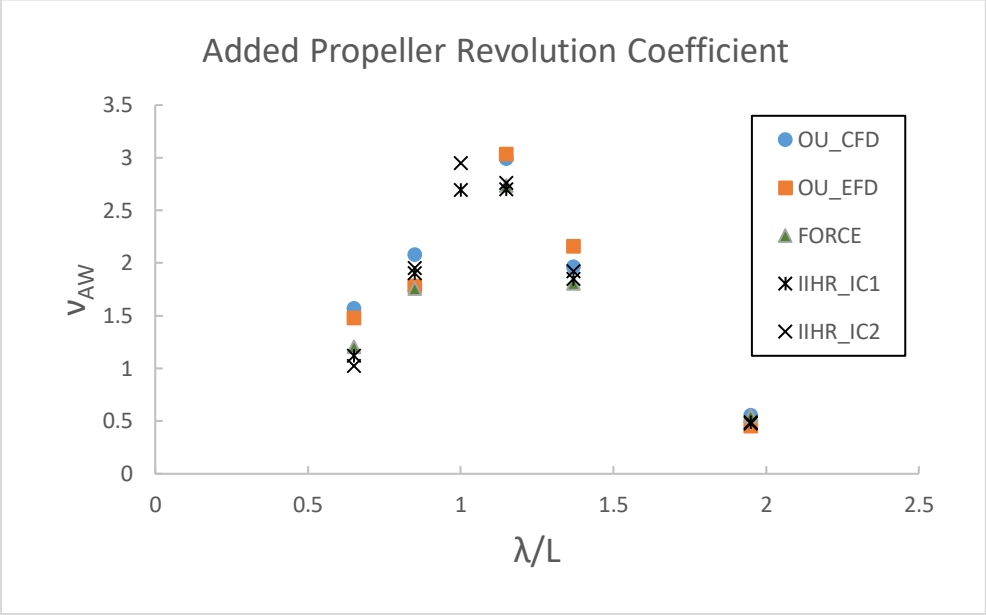

Figure 51: Added propeller revolution coefficient

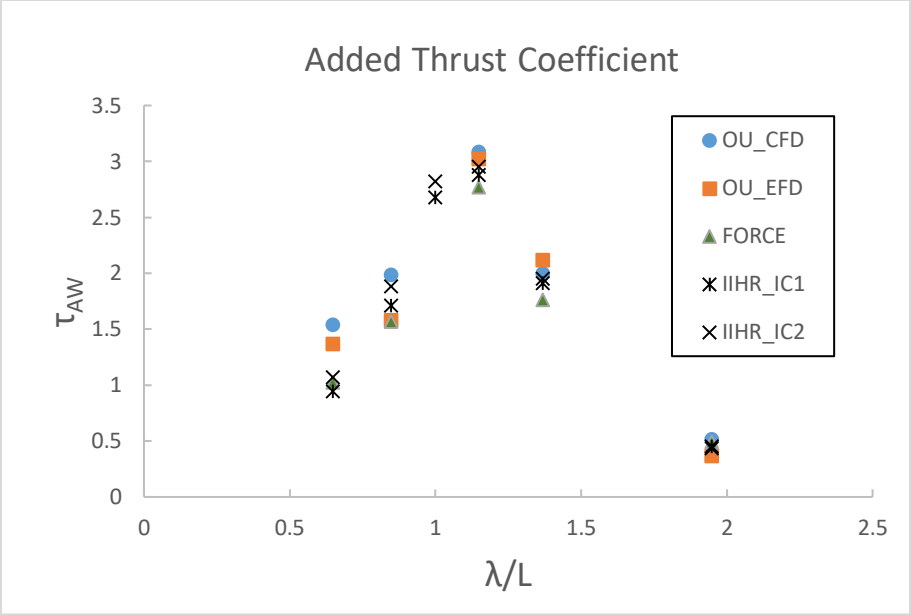

Figure 52: Added thrust coefficient

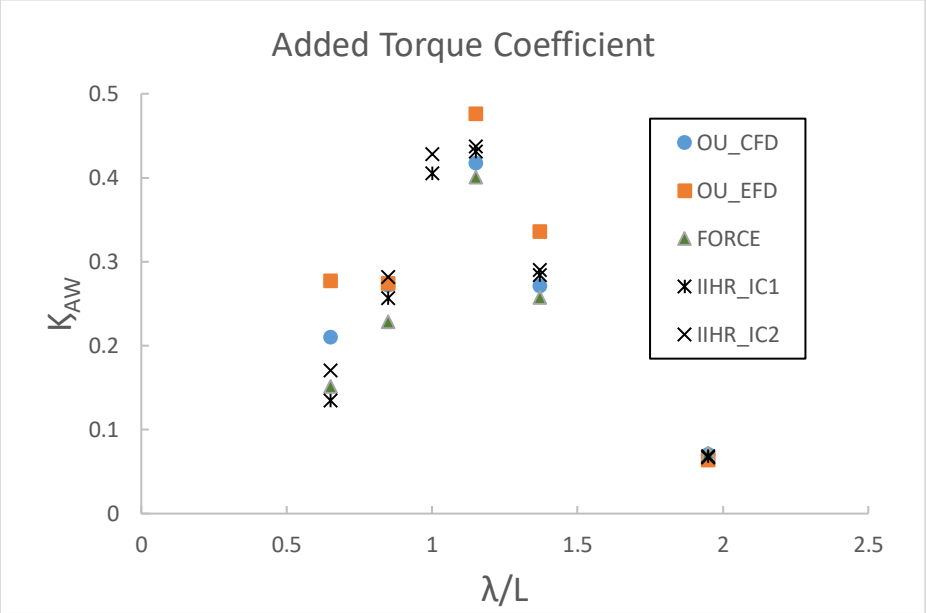

Figure 53: Added Torque Coefficient

Chapter 6: Conclusions

Resistance, self-propulsion, and detail flow field analysis in calm water and in waves had been conducted successfully by CFD and EFD method. In this study, heave and pitch motions as well as the added resistance have been predicted for KCS model at Fn=0.26 in head wave conditions by CFD and EFD. The comparison in time history shows a very small phase lag between the predicted motions and EFD measurement. Predicted heave and pitch motions show good agreement with the EFD measurement done at Osaka University as well as with other experimental data. Added resistance prediction shows similar trend between CFD and EFD. Especially, the peak has been predicted by both methods at the same wavelength. The predicted motions and added resistance show good agreement with EFD data, which reveals that the CFDSHIP-IOWA solver is good enough to make reliable prediction for high speed container ship.

The nominal wake at propeller plane in waves has been analyzed in detail. Predicted velocity distribution at propeller plane shows good agreement with S-PIV measurement. The bilge vortex and the secondary vortex has been observed. Both vortex system rotates in opposite directions to each other. It has been observed that the predicted bilge vortex stays on the side and upper part of the dummy boss but never goes underneath the dummy boss due to the fine stern shape of KCS.

At first, the study has been carried out without the propeller model, but with a dummy propeller boss. Later, body force propeller model has been included to predict the effective wake. S-PIV measurements have been carried out after the rudder for the self-propulsion condition. Computed nominal wake and measured effective wake both shows similar trend and are almost sinusoidal.

For the mean thrust and torque, CFD and EFD have good agreement. Compared to KVLCC2, KCS has smaller block coefficient. Thus, in waves the bilge vortex moves inside the propeller radius with smaller vorticity magnitude. The oscillation of nominal and effective wake factor can be treated as a simple harmonic. For detail flow field, CFD and EFD (S-PIV) have good agreement for flow pattern. In the propeller upstream, the flow pattern is influenced by the relative velocity of stern upward flow and stern vertical motions. Because of right-rotating propeller in stern upward flow, the starboard u/U is higher than portside u/U. Interfered by the rudder leading edge, the flow

would be accelerated in upper starboard and lower port-side. The hub vortex was separated into two cores. In the rudder downstream, the cross flow was twisted and forms upward flow portside and downward starboard. The flow pattern moves up and down relative to the stern vertical motions. As concluded in Sadat-Hosseini, et al. (2013) for KVLCC2, the present work proves the capability of EFD and CFD to provide the flow field measurement and simulation although those methods are much costly than potential flow-based method. For the future work, the phase issue will require a thorough investigation. In addition, for industrial and practical application, large y+ and smaller grid numbers should be studied for CFD.

References

(2010). Retrieved from Pointwise, Gridgen: http://www.pointwise.com/

(2015, December 2-4). Retrieved from Tokyo Workshop on CFD in Ship Hydrodynamics: http://www.t2015.nmri.go.jp/index.html

(2015, December 2-4). Retrieved from KCS (Case_2.10) : http://www.t2015.nmri.go.jp/Instructions_KCS/Case_2.10/Case_2-10.html

(2015, December 2-4). Retrieved from KCS (Case_2.11) : http://www.t2015.nmri.go.jp/Instructions_KCS/Case_2.11/Case_2-11.html

Carrica, P. M., Wilson, R. V., Noack, R., Xing, T., Kandasamy, M., Shao, J., . . . and Stern, F. (2006). A Dynamic Overset, Single-Phase Level Set Approach for Viscous Ship Flows and Large Amplitude Motions and Maneuvering. *26th Symposium on Naval Hydrodynamics.* Rome, Italy.

Carrica, P., Fu, H., & and Stern, F. (2011). Computations of self-propulsion free to sink and trim and of motions in head waves of KCS model. *Journal of Applied Ocean Research, 33(4)*, 309-320.

Castro, A., Carrica, P., & and Stern, F. (2011). Full scale self-propulsion computations using discretized propeller for KCS. *Journal of Computers & Fluids, 51(1)*, 35-47.

Filip, G., Xu, W., & and Maki, K. (2017). *URANS predictions of resistance and motions of the KCS in head waves.* Technical Report, No. 355, University of Michigan.

Gaggero, S., Villa, D., & and Viviani, M. (2015). The KCS test case: an open source overview. *International Conference on Computational Method in Marine Engineering.* Rome, Italy.

Gerritsma, J., & & Beukelman, W. (1972). Analysis of the resistance increase in waves of a fast cargo ship. *International Shipbuilding Progress, 18* .

Havelock, T. (1942). Drifting force on a Ship in Rough Seas. *Philosophical Magazine, 33*.

Hossain, M. A., Wu, P.-C., Shibano, Y., & Toda, Y. (2018). Forces, Ship Motions and Velocity Wake Field for KRISO Container Ship Model in Regular Head Waves. *Conference Proceedings of 28th International Ocean and Polar Engineering Conference (ISOPE 2018)*. Sapporo, Japan: International Society of Offshore and Polar Engineers.

Maruo , H. (1963). Resistance in waves. *60th anniversary Series, The Society of Naval Architects of Japan, 8*, 67–102.

Maruo, H. (1957). The excess resistance of a ship in rough seas. *International Shipbuilding Progress, 4 (35)*.

Menter, F. (1994). Two-Equation Eddy Viscosity Turbulence Models for Engineering Applications. *AIAA Journal, 32*, 8.

Nakamura, S., & Naito, S. (1975). Propulsive performance of a container ship in waves. *Journal of Kansai Society of Naval Architects of Japan, 159*.

Ozdemir, Y., Cosgun, T., Dogrul, A., & and Barlas, B. (2016). A numerical application to predict the resistance and wave pattern of KCS. *Brodogradnja/Shipbuilding, 67(2)*, 47-65.

P.-C., W., Hossain, M. A., Kawakami, N., Tamaki, K., Kyaw, H., Matsumoto, A., & Toda, Y. (2020, March). EFD and CFD Study of Forces, Ship Motions and Flow Field for KRISO Container Ship Model in Waves. *Journal of Ship Research, Vol. 64*(No. 1), pp. 61-80.

Paterson, E. G., W., R. V., & and Stern, F. (2003). *General purpose parallel unsteady RANS ship hydrodynamics code: CFDSHIP-IOWA.* Technical Report, No. 432, University of Iowa, IIHR, Iowa, USA.

Sadat-Hosseini, H., Sanada, Y., Stocker, M., Stern, F., Toxopeus, S., Castiglione, T., . . . Otzen, J. F. (2015). KCS Added Resistance for Variable Heading. *Workshop on CFD in Ship Hydrodynamics.* Tokyo.

Sadat-Hosseini, H., Wu, P., Carrica, P., Kim, H., & Toda, Y. (2013). CFD verification and validation of added resistance of KVLCC2 with fixed and free surge conditions in short and long head waves. *Journal of Ocean Engineering, Vol. 59*.

Simonsen, C. D., Otzen, J., Joncquez, S., & Stern, F. (2013). EFD and CFD for KCS heaving and pitching in regular head waves. *Journal of Marine Science and Technology*.

Tezdogan, T., Demirel, Y., Kellett, P., Khorasanchi, M., Incecik, A., & and Turan, O. (2015). Full-scale unsteady RANS CFD simulations of ship behavior and performance in head seas due to slow steaming. *Journal of Ocean Engineering, 97*, 186-206.

Tokgoz, E., Win, Y. N., Kuroda, K., & Toda, Y. (2014). A New Method to Predict the Propeller Body Force Distribution for Modeling the Propeller in Viscous CFD Code without Potential Flow Code. *Journal of the Japan Society of Naval Architects and Ocean Engineers, 19*, pp. 1-7.

Wilson, R. V., Carrica, P. M., & and Stern, F. (2006). Unsteady RANS method for ship motions with application to roll for a surface combatant. *Computers & fluids, Vol.35*(Issue 5), pp.501-524.

Wu, P. C. (2013). *A CFD Study on Added Resistance, Motions and Phase Averaged Wake Fields of Full Form Ship Model in Head Waves.* Osaka: Osaka University.

Wu, P.-C., Sadat-Hosseini, H., Stern, F., & and Toda, Y. (2017). Nominal wake fluctuation due to waves: volume mean and distribution based on CFD and PIV. *Conference Proceeding of The Japan Society of Naval Architect and Ocean Engineering, Vol. 24*, p. pp. 1.

Wu, P.-C., Tokgoz, E., Okawa, H., Tamaki, K., & and Toda, Y. (2016). Computational and Experiment of Propeller Performance and Flow Field around Self-propelled Model Ship in Regular Head Waves. *Proceedings of the 31st Symposium on Naval Hydrodynamics.* Monterey, California.

Xing, T., Carrica, P., & and Stern, F. (2008). Computational towing tank procedures for single run curves of resistance and propulsion. *Journal of Fluids Engineering, Vol.130*(Issue 10), pp. 101-102.

Yamazaki, R. (1977). On the Propulsion Theory of Ships on Still Water (Improved Theoretical Method). *Vol. 34*, pp. pp. 65-88.

Yokota, S. (2013). *The simple prediction method for body force distribution in CFD code.* B.S. thesis (in Japanese), Osaka University.